The Thesis Committee for Wesley James Ahearn
Certifies that this is the approved version of the following thesis

Spectroscopic Studies of Boron Carbo-Nitride

APPROVED BY
SUPERVISING COMMITTEE:

Supervisor:

John G. Ekerdt

Gyeong S. Hwang

Spectroscopic Studies of Boron Carbo-Nitride

by

Wesley James Ahearn, B.S., Ch.E.

Thesis

Presented to the Faculty of the Graduate School of
The University of Texas at Austin
in Partial Fulfillment
of the Requirements
for the Degree of

Master of Science in Engineering

The University of Texas at Austin
December 2010

Dedication

For my wife and my parents

Acknowledgements

I would like to thank my advisor. Dr. John Ekerdt has supported me for many years. I am especially thankful to him for the opportunity to pursue graduate studies. He has been a source of guidance and advice through a difficult time in my life.

I must also thank the colleagues that have helped me along the way. Ward Engbrecht was responsible for much of the fundamental research of boron carbo-nitride films. He provided me with valuable insight and taught me useful techniques in vacuum science. Ryan Fitzpatrick was my lab mate for many years. His outstanding work ethic and positive attitude made working with him a pleasure. I am thankful for the equipment time he yielded willingly. Luke Henderson patiently provided guidance with electrical testing and processing steps for metallization. I had many insightful discussions with Michael Ramon and his help regarding the troubleshooting of electrical testing was much appreciated. Other researchers I would like to thank include Tuo Wang, Wyatt Winkenwerder, Scott Stanley, Andy Lemonds, and all of the Ekerdt group members I have known.

Certain individuals were instrumental in the collection of data within this thesis. I must thank Sean King for FTIR measurements and valuable discussions regarding my research. Nathalie Valle was helpful in analyzing SIMS samples as well as facilitating the use of other hydrogen detecting methods.

The University staff has been very helpful. I would like to thank Jim Smitherman, Butch Cunningham, Kevin Haynes, Eddie Ibarra, T. Stockman, and Rico Garcia, among others.

Lastly, I would like to thank my wife, Ruth. She has been beside me every step of the way along this journey. She never gave up on me and because of that, I never gave up on myself. She has been a pillar of strength, and I am forever grateful to have her in my life.

September 8, 2010

Abstract

Spectroscopic Studies of Boron Carbo-Nitride

Wesley James Ahearn, M.S.E.
The University of Texas at Austin, 2010

Supervisor: John G. Ekerdt

BC_xN_y films were characterized as a potential pore sealing layer for low κ dielectrics. The changes in chemical bonding were studied as a function of growth temperature to aid in understanding the variation in electrical performance of these films. Thermal chemical vapor deposition of BC_xN_y using dimethylamine borane and ethylene were deposited on porous methylsilsesquioxane substrates at 335 °C and 1 Torr. BC_xN_y was able to seal the porous interface with a thickness of 3.9 nm for both blanket and patterned substrates. BC_xN_y films deposited over a temperature range of 300-400 °C with dimethylamine borane and either ethylene or ammonia coreactant gas were characterized. Films deposited with ethylene became more concentrated in B at the expense of C with increasing temperature. These films favored C-B intermixing over C-C and B-B bonding at higher temperature. H was detected in the form of B-H and C-H bonds. Films deposited with ammonia became concentrated in N at the expense of B, and favored B-N bonding at higher temperatures. H was found in the films as B-H, C-H, and N-H bonds. The amount of H in the films decreased with increasing growth temperature for both ethylene and ammonia coreacted films. The valence band offset of C-rich films increased from 0.17 ± 0.22 eV to 0.32 ± 0.22 eV when deposited at 300°C and 400 °C. For the N-rich films, the valence band offset shifted from 0.26 ± 0.28 at 300 °C to -0.15 ± 0.24 eV at the same deposition conditions. High temperature annealing from 400-800 °C in forming gas caused all BC_xN_y films to decrease in thickness up to 30%. At the same time, the index of refraction increased, and likely, the dielectric constant. X-ray photoelectron spectroscopy revealed little change in the constituent bonding, suggesting that volatile –H containing species were removed during the annealing process.

Table of Contents

List of Tables

List of Figures

List of Illustrations

Chapter 1: Introduction

1.1. OVERVIEW

The microelectronics industry continues to aggressively scale down the dimensions on semiconductor devices. Historically, the industry has followed a trend known as Moore's Law. This trend states that the number of transistors on a device will double roughly every two years. While Moore originally predicted this trend would continue for 10 years, it has become an industry goal, and has held for over 50 years.

The capability to increase the number of devices on an integrated circuit is made possible by the continued scaling of device dimensions. Early on, advances were made without having to change the basic materials used in semiconductor manufacturing. In the mid 1990s a major impediment to Moore's law developed due to this scaling. While dimensions were reduced at the front end of devices, the back end dimensions were also reduced to accommodate increased device density. Before the 0.5 – 0.25 µm technology node the performance improved with reduced device dimensions due to the reduced delay at the gate. Upon reaching these dimensions, the back end signal delay became an important factor in device performance.

Signal delay in the interconnect is known as resistive-capacitive (RC) delay, and is associated with the propagation of electric signals along conductive lines that are isolated from one another by a dielectric. The resistive part of the delay is determined by the dimensions and the resistivity of the conductor. The capacitive part of the delay is governed by the interconnect dimensions, the dielectric thickness, and the relative dielectric constant of the insulator. The cross section of an interconnect structure is presented in Illustration 1.1 [1].

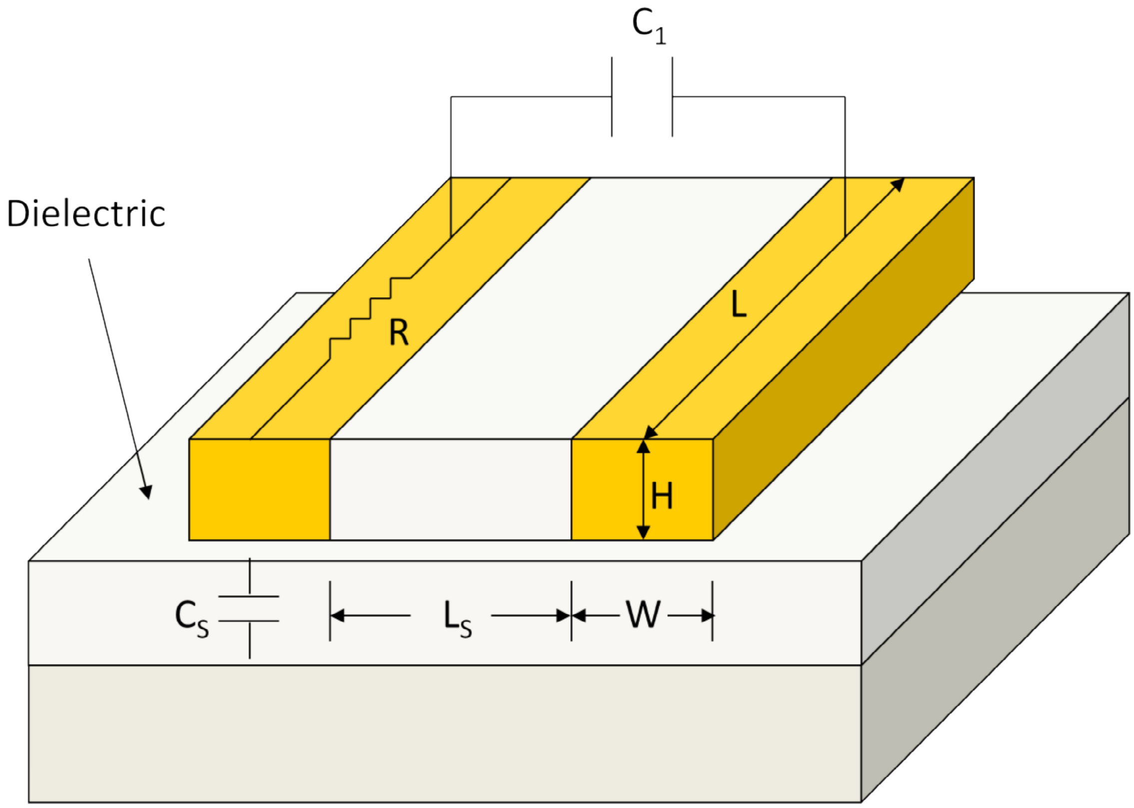

Illustration 1.1. Cross section of an interconnect structure and the associated losses and dimensions that govern the RC delay [1].

The total RC delay associated with one of the interconnect lines is represented by the following equation:

$$\tau = \kappa_d \varepsilon_0 \rho L^2 \left(\frac{1}{Hd} + \frac{1}{WL_s} \right) \tag{1.1}$$

where κ_d is the relative dielectric constant of the insulator, ε_0 is the permittivity of free space, ρ is the resistivity of the conductor, L is the length of the conductive line, H is the interconnect height, W is the interconnect width, d is the thickness of the dielectric layer, and L_s is the spacing between conducting lines. Note that the dimensions H, d, W, and L_a shrink with each technology node.

For the semiconductor industry, the way forward was found in lowering the resistivity and the dielectric constant of the interconnect system. This was realized by changing the materials traditionally used in integrated circuits, along with architectural changes in the interconnect. The latter was borne out of the planarization process, which enabled an increase in the number of metal wiring layers, providing a design that could minimize wiring lengths in a given area [2].

To lower the resistivity of the conducting line, Cu was employed instead of Al. The bulk resistivity of Cu is 1.68 μΩ cm, about 60% of that of Al. An added bonus of replacing Al with Cu was that the electromigration performance of Cu was superior. The change did not happen seamlessly, though. Two major difficulties with using Cu in semiconductor devices are that Cu is a fast diffuser in Si and SiO_2 and that Cu is difficult to dry etch anisotropically in comparison to Al [2]. The answer to the etching problem was found in the dual damascene process, which also allowed for increased metallization levels. To prevent Cu from reaching the dielectric material, a diffusion barrier was necessary.

Using the dual damascene process it was possible to etch vias and lines in SiO_2, deposit a liner diffusion barrier, plate copper, polish the metal to planarize it, and cap the metal with another diffusion barrier material. With this method, Cu was integrated into the process and devices continued to scale down. The relief was short-lived, however, as Cu is among the lowest resistivity metals and Moore's Law pushed ahead.

Further reduction in the RC delay required the use of an insulator with a lower dielectric constant than that of SiO_2 ($\kappa = 3.9$). The factors that influence the dielectric constant of a material can be seen in the Debye equation [2]:

$$\frac{\kappa-1}{\kappa-2}=\frac{4\pi}{3}N\left(\alpha_e+\alpha_d+\frac{\mu^2}{3k_bT}\right) \tag{1.2}$$

N is the density of dipoles, α_e and α_d are the electronic and distortion polarizations, μ is the dipole moment, k_b is the Boltzmann constant, T is the temperature, and κ is the dielectric constant of the material. It is seen that the dielectric constant is a function of the density of dipoles and the various polarizations of the material; these are the three terms in parentheses, the third being the orientation polarization.

From the Debye equation it is evident that to lower the dielectric constant of a material, either the density or polarizability of the dielectric must be reduced. Because device operating frequencies are typically in the MHz to GHz range, all three polarizability terms are important and efforts should be made to minimize them. The more tightly bound the electrons in a bond, the less electronic polarization can occur. Delocalized bonds, such as double and triple bonds, are highly polarizable. Note that there is an inverse relationship between the bond strength and the electron polarizability, as single bonds are among the weakest [3].

The distortion and orientation polarizations are also known as the nuclear response and are affected by both permanent and transient dipoles. Polar constituents in the material, such as hydroxyl and carbonyl groups, contribute to the nuclear response. Moisture incorporation into the dielectric also increases the nuclear response due to the large permanent dipole of water [3].

Beside reducing the dipole moment of atomic bonds and limiting the delocalization of electrons in the material, the dielectric constant may also be lowered by reducing the density of the material. Since every material has a dielectric constant relative to free space, the removal of that material must lower the dielectric constant. There are two main ways to reduce the density of a material. The replacement of atoms by bulky ligands such as CH_3 and H in a silica network allows for substantially less density. These materials are the spin on glasses. Alternatively, a porogen may be used to incorporate nanometer sized pockets of air into the material. Potentially the best strategy would involve using an already low κ material and pairing it with a porogen technique, lowering the amount of voids needed to attain a desired dielectric constant. This is important as more air incorporation weakens the thermal and mechanical stability of the material.

SiO_2 is a remarkable material. Its thermal, mechanical, and electrical properties have all contributed to making SiO_2 a primary material in the history of semiconductor processing. The properties that make it such a good insulating material for semiconductors are not easily found together in other materials. At best, the replacement of SiO_2 results in a trade-off of performance in another area for improved dielectric constant. In the case of low κ dielectrics based on organic hydrocarbons, it is desirable that the bonds are aliphatic to lower the polarizability, yet saturated bonds are not as thermally stable as conjugated bonds, and will not survive the thermal processing steps necessary in semiconductor manufacture [4]. Therefore, thermal stability is the limiting factor in the dielectric constant with these materials. Further reduction in the permittivity must come from reduction in density by the inclusion of pores.

The pore structure of a low κ material can adversely affect its mechanical strength as well as its adhesion to other materials. It also makes the material susceptible to penetration by chemicals during other processing steps in the formation of the interconnect.

So while the introduction of Cu and low κ materials has allowed for the continued reduction in device dimensions, it has also created many material integration problems, the most important being the need for a Cu diffusion barrier and a pore sealing layer for the low κ. A diffusion barrier must be continuous and uniform, and on the order of a few nm thick. Coating a porous material with a diffusion barrier is non-trivial. If the average pore size and connectivity are large, it may take an unacceptably thick layer to cover the surface [4].

1.2. CURRENT IC TECHNOLOGY

1.2.1. Cu Liner and Cap

The standard cap for Cu damascene structures is a dielectric. Isolation is required between layers of metallization. Si_3N_4 was used as the inter layer diffusion barrier because it effectively prevented Cu diffusion. Recently SiC_x and SiC:H have replaced this material in an effort to further lower RC delay [5]. The dielectric constants of these materials have been reported as low as 4.8 and 4.5, respectively, and the κ of SiC_x is further reduced by adding N [6,7]. Still lower dielectric constant values are needed for future technology nodes. One strategy has been the attempted use of a metal barrier as the Cu cap. An added bonus of using a metal barrier layer as the ILD is improved electromigration resistance due to increased adhesion between the Cu and the barrier layer [8]. However, the use of a metal layer may still require the use of a dielectric capping layer as integrating a standalone metal barrier into the process requires significant changes to existing techniques. The metal layer would also have to withstand various processing chemistries after deposition and function as a moisture barrier. These metal capping layers are either Co or Ni alloys and are formed by electroless deposition, preferentially depositing on the Cu [9].

A combination metal alloy/dielectric cap sandwich structure may ultimately be required in future technology nodes. The metal alloy electromigration performance enhancement is due to enhanced adhesion at the interface. The activation energy for electromigration is directly related to the adhesion, and the adhesion to Cu for CoWP is about 30% greater than that of SiC_xN_y [9]. Techniques have been reported to enhance the adhesion between Cu and the dielectric capping layer. Typically, the Cu is treated in the deposition chamber with RF plasma before dielectric deposition to clean the surface. In addition, silane treatment has been used to form graded interfaces [10]. Takewaki, *et al.*, reported that Cu interconnects passivated with a CuSi layer have a doubled lifetime [11]. Similarly, Gosset, *et al.*, achieved median time to failure increased by a factor of 2 and 9, with a $CuSiC_xN_y$ mixing zone, compared to standard SiN_x and SiC_x barriers, respectively [12].

The liner material between Cu and the inter-metal dielectric is a composite PVD Ta/TaN layer. The TaN is deposited first, providing good adhesion to the dielectric and superior Cu barrier performance. Ta is then deposited on top of the TaN to provide good adhesion to Cu. The drawbacks to PVD deposition are poor step coverage and increased resistivity [13]. Ru has been investigated as a potential barrier/ Cu seed layer. The electrical resistivity of Ru is 7.6 $\mu\Omega$ cm, approximately half that of Ta [14] and it has been successfully deposited by CVD. The barrier capabilities of Ru are poor, owing to the columnar growth of these films. Amorphous Ru(P) films outperformed PVD TaN in bias temperature stress tests of metal oxide semiconductor capacitor structures over a range of electrical fields and elevated temperatures [15]. Ru-B-C films were found to be amorphous to 700 °C and thermally stable up to 750 °C [16].

1.2.2. Porous Low κ Materials and Pore Sealing Layers

Amorphous, hydrogenated silica was the standard BEOL dielectric until the introduction of fluorosilicate glass. The formation of Si-F bonds reduced the dielectric constant through the lowering of bond polarizability relative to Si-O, though the decrease in κ was minimal (3.6-3.8) [2]. The next attempt at low κ materials involved amorphous carbon films. This term encompasses a wide variety of materials composed of sp^1, sp^2, and sp^3 bonding arrangements. The hydrogen concentration (C_H) of these films is determined by the precursor and deposition conditions, and may vary from 1 to 50%. Low ion energy plasmas (<50 eV) produce sp^3 hybridized carbon films with the highest H concentrations. For higher ion energies, the films are hard, and composed of approximately 60% sp^2 hybridized bonds, with less H incorporation. At ion energies above 100 eV, the films are classified as tetrahedral amorphous carbon, and consist of sp^3 bonds and < 1% H [17].

Diamond-like carbon (DLC) films have been deposited using a variety of plasma assisted or plasma enhanced CVD processes. For DLC films, the C_H is inversely related to the dielectric constant and the refractive index. The main problem associated with DLC films is their lack of thermal stability to 400 °C. The attempted solution was to incorporate C-F bonds into the films, and thermally stable (as determined by step height measurement and Rutherford backscattering spectroscopy), fluorinated DLC films were synthesized with κ < 2.7 [18]. Unfortunately, the F present in these films is able to react with Ta in the barrier layer and induce delamination.

PECVD SiCOH materials were successfully implemented into IBM 90 nm and 65 nm technology nodes. Spin on materials suffered from mechanical stability issues. The most popular PECVD precursors were diethoxymethylsilane (DEMS) and tetramethylcyclotetrasiloxane (TMCTS) because they did not suffer from oxidation of C-H bonds since there were more Si-O bonds contained in the precursor structure [2].

For the 45 and 32 nm node, device performance requires dielectrics with κ from 2.4-2.2. To achieve these values, air must be incorporated into the material. Thus the film porosity, defined as the ratio of the void volume to solid volume, governs the reduction in polarization by reducing overall film density.

These materials are generally deposited by either PECVD or spin on methods. The choice has narrowed to DEMS as a suitable SiCOH precursor for the PECVD process. The minimum κ achievable for porous DEMS has been 2.2 [19]. Pores are introduced into PECVD material via three pathways: silicate network modification by choice of precursor, chemical modification by post treatment, or removal of a labile phase known as a porogen. The current technique for large scale manufacturing involves use of a porogen, which can be removed either thermally over a number of hours or thermally with UV irradiation for a faster curing time.

The leading spin on material is SiLK, a polyarylene with exceptional thermal stability and good electrical properties. SiLK must undergo a thermal curing process above 325 °C, where an acetylene crosslinking reaction takes place, allowing for better mechanical strength of the film. This is an essential step with the addition of a porogen. Thus the porogen must have a high decomposition temperature such that the SiLK will not collapse due to capillary pressure before curing. By using cross-linked polystyrene nanoparticles with a small size distribution, the pore size was optimized to a mean pore diameter of 5 nm [20]. Porous SiLK is the only porous organic polymer that has been tested in BEOL integration studies.

The addition of these porous low κ materials has resulted in significant challenges for integration. Depositing the ILD on the capping layer is complicated by adhesion issues. The adhesion is inversely proportional to the porosity. One strategy is to deposit a dense ILD at the interface. Line bottom roughness is introduced at the bottom of the via during processing steps involving oxidative plasmas. This damage is also extended to the sidewalls. The roughness caused by these processing steps coupled with the increased porosity of lower dielectric constant materials results in the need for thicker Cu diffusion barrier layers to fully protect the dielectric.

A number of pore sealing strategies have been reported in the literature. Plasma treatment has been used to selectively target the first few nm near the surface of the low κ. By tailoring the plasma chemistry, densification of the material is possible. This technique has had the most success with microporous materials. Mesoporous dielectrics are damaged much more deeply, due to pore interconnectivity. Chang, *et al.*, [21] found that a mesoporous silica film treated with Ar and O_2 plasma had a densified layer <20 nm thick. Posseme, *et al.*, found complete bulk modification of a highly porous SiCOH film after oxidizing plasma exposure with FTIR measurements showing a large peak shift of the Si-O-Si band and the appearance of a peak in the 3000 to 3700 cm^{-1} region attributed to moisture uptake [6]. These plasma densified layers may also be susceptible to wet etching introduced later in the process flow. Broussous, *et al.*, demonstrated that plasma treated methyl silsesquioxane (MSQ) with a surface densified layer of 10.9 nm was etched nonlinearly with exposure time to a wet dilute HF process [22]. The thickness of the layer was monitored with spectroscopic ellipsometry.

The other commonly used strategy to seal pores is the deposition of a capping or sealing material. These layers may be deposited by CVD or spin on methods, and the layers themselves may be organic or inorganic. Two potential complications associated with this method are the introduction of new interfaces that may suffer from adhesion problems and increasing the overall dielectric constant of the combined dielectric/capping layer [2]. It is important to choose a sealing material with as low a κ as possible.

One material that may function as a potential pore sealer/Cu diffusion barrier and Cu cap is boron carbo-nitride (BC_xN_y, or BCN). Engbrecht, *et al.*, published a series of papers reporting the growth and characterization of BCN either from a single source precursor, dimethylamine borane complex [$NH(CH_3)_2{:}BH_3$] [23], or coreacted with ammonia [NH_3] and ethylene [C_2H_4] [24]. The dielectric constant of these films, deposited at 360 °C and at a pressure of 1 Torr, was 4.62 without coreactant. This value decreased to 4.11 with the addition of ammonia and was further reduced to 3.66 with simultaneous dosing of ammonia and ethylene. BCN with the same dielectric constant was achieved without ammonia by adjusting the ethylene flow rate [24]. The films were found to be amorphous by x-ray diffraction (XRD). The copper diffusion barrier properties of BCN on blanket thermal oxide films were investigated by time dependent dielectric breakdown (TDDB) of metal oxide semiconductor (MOS) capacitor structures, and compared to SiC_xN_y, a commonly used industrial cap material [25]. The ethylene coreacted BCN films had the best leakage current performance at 0.5 MV/cm (1.12×10^{-8} A/cm^2) [25] compared to BCN deposited with ammonia or without coreactant gas. The leakage current of BCN was higher than SiC_xN_y (5.5×10^{-9} A/cm^2) [24] for every BCN film tested. Devices were bias stress tested at 150°C in N_2 ambient at electric field values of 2-5 MV/cm. The ethylene coreacted BCN film failure times are on the order of SiC_xN_y, and performed better at higher field values than SiC_xN_y. The leakage current results coupled with the TDDB test suggests that carbon rich BCN films of composition $BC_{0.90}N_{0.08}$ are as effective as a SiC_xN_y Cu capping layer.

BCN has been reported with a κ as low as 2.1 [26]. This is important as it does not significantly raise the overall dielectric constant of the BCN/low κ system. These films were deposited by plasma enhanced CVD of tris(dimethylamino)boron at a deposition temperature of 350 °C and RF power of 20-100 W. Sugiyama, *et al.*, reduced the dielectric constant of BCN films by thermal annealing post deposition. Samples with a range of dielectric constants were annealed from 5 to 15 min at 400 °C, and the ratio of the dielectric constant measurements before/after annealing ranged from 0.64 – 0.84, and was independent of annealing time [27].

Though the replacement of the Ta/TaN and SiN_x layer with BCN alone is unlikely, its ability to function as a pore sealing layer has been investigated. Additionally, the bonding of these films has been investigated as a function of growth temperature and coreactant gases to elucidate why the films behave better electrically when deposited with NH_3 at low temperature.

1.3. OBJECTIVE AND OVERVIEW OF CHAPTERS

The objective of the work presented here is to gauge the potential of BCN for use as an insulating and pore-sealing layer. Chapter 2 focuses on sealing porous MSQ substrates with varying thickness BCN. Chapter 3 investigates the change in bonding within these films as deposition temperature and reaction gases are varied. The BCN/Si(100) heterojunction is described by x-ray photoelectron spectroscopy (XPS) valence band measurements. High temperature annealing is performed in an attempt to lower the dielectric constant of a variety of BCN film compositions. A summary of the work and suggestions for future work are discussed in Chapter 4.

In Chapter 2, the pore sealing ability of BCN was studied with the BCN/pMSQ system. Amorphous boron carbo-nitride films were deposited on blanket etched and ashed pMSQ/Si substrates at a temperature of 335 °C using dimethylamine borane

[$NH(CH_3)_2$:BH_3] vaporized in a bubbler held at 41 °C with Ar carrier gas and ethylene [C_2H_4] coreactant gas. BCN film thicknesses ranged from 1.8 to 40.6 nm. Following the deposition, samples were heated to 230 °C, exposed to TaF_5 for 60s, and cooled in Ar. After exposure the films were depth profiled by XPS and backside secondary ion mass spectrometry (SIMS) to determine the penetration depth of the TaF_5. BCN was able to prevent penetration of TaF_5 into the pMSQ at a minimum thickness of 3.9 nm on blanket films. A separate set of films were deposited on patterned pMSQ substrates. $TaSi_x$ films were deposited on the BCN/pMSQ samples and electron energy loss spectroscopy was used to determine the composition across sidewall features. The attenuation of the Ta signal before the BCN/pMSQ interface confirmed that 3.9 nm films were sufficient to seal a sample patterned similarly to what would be found in a dual damascene process.

In Chapter 3, the bonding within BCN films is studied as a function of deposition temperature and coreactant gas. BCN films were deposited at substrate temperatures from 300-400 °C using dimethylamine borane and either ethylene or ammonia. Samples were analyzed by SIMS and Fourier transform infrared spectroscopy (FTIR) to reveal the –H bonding in the films. The valence band offset of the BCN/Si(100) heterojunction was measured by XPS to aid in understanding the electrical characteristics of boron carbo-nitride. The H content of the films was found to decrease for both C-rich and N-rich films with increasing deposition temperature. N-rich films contained roughly twice the relative H as C-rich films deposited at 300 °C. For N-rich films, the composition became poorer in B and richer in N at higher temperature. A shift from B-B to B-N bonding was found from peak deconvolution of the B 1*s* spectra of these films. The C-rich films became B-rich and N-poor with increasing temperature. C-B and B-C bonding increases at the expense of C-C and B-B bonding. The valence band offset for BCN/Si(100) ranged from 0.17 to 0.32 eV for C-rich films and from 0.26 to -0.15 eV for N-rich films, deposited at

300 °C and 400 °C. Forming gas anneals of C-rich and N-rich BCN resulted in a thickness loss of up to 30% and an increase in index of refraction for all films. The thickness change scaled with H content of the films.

1.4. REFERENCES

[1] Plummer, J.D., Deal, M.D., Griffin, P.B. Silicon VLSI Technology Fundamentals, Practice and Modeling. Upper Saddle River, NJ: Prentice Hall; 2000.

[2] Volksen, W., Miller, R.D., Dubois, G. *Chem. Rev.*, 82, pp. 56-110; 2010.

[3] Morgen, M., Ryan, E.T., Zhao J.-H., Hu, C., Cho, T., Ho, P.S. *Annu. Rev. Mater. Sci.*, 30, pp. 645-680; 2000.

[4] Baklanov, M.R., Maex, K. *Phil. Trans. R. Soc. A*, 364, pp. 201-215; 2006.

[5] Chiang, C.-C., Wu, Z.-C., Wu, W.-H., Chen, M.-C., Ko, C.-C., Chen, H.-P., Jang, S.-M., Yu, C.-H., Liang, M.-S. *Jpn. J. Appl. Phys.*, 42, pp. 4489-4494; 2003.

[6] Posseme, N., Chevolleau, T., David, T., Darnon, M., Louveau, O., Joubert, O., *J. Vac. Sci. Technol. B*, 25, pp. 1928-1940; 2007.

[7] Cheng, Y.-L., Chen, S.-A., Chiu, T.-J., *J. Vac. Sci. Technol. B*, 28, pp. 573-576; 2010.

[8] Nakano, H., Itabashi, T., Akahoshi, H., *J. Electrochem. Soc.*, 152, pp. C163-C166; 2005.

[9] Gambino, J., Wynne, J., Gill, J., Mongeon, S., Meatyard, D., Lee, B., Bamnolker, H., Hall, L., Li, N., Hernandez, M., Little, P., Hamed, M., Ivanov, I., Gan, C.L., *Microelectronic Engineering*, 83, pp. 2059-2067; 2006.

[10] Gosset, L.G., Chun, S., Farcy, A., Casanova, A., Arnal, V., Besling, W.F.A., Torres, J., *Proceedings of the IEEE International Interconnect Technology Conference*, 7-9 June 2004, pp. 15-17; 2004.

[11] Takewaki, T., Yamada, H., Shibata, T., Ohmi, T., Nitta, T., *Proceedings of the International Symposium on Power Semiconductor Devices and ICs*, 23-25 May 1995, pp. 438-442; 1995.

[12] Hohage, J, Lehr, M.U., Kahlert, V., *Microelectronis Engineering*, 86, pp. 408-413; 2009.

[13] Choi, B.H., Lim, Y.H., Lee, J.H., Kim, Y.B., Lee, H.-N., Lee, H.K., *Microelectronic Engineering*, 87, pp. 1391-1395; 2010.

[14] Wang, Q., Ekerdt, J.G., Gay, D., Sun, Y.-M., White, J.M., *Appl. Phys. Lett.*, 84, pp. 1380-1382; 2004.

[15] Henderson, L.B., Ekerdt, J.G., *Thin Solid Films*, 517, pp. 1645-1649; 2009.

[16] Perng, D.-C., Yeh, J.-B., Hsu, K.-C., Wang, Y.-C., *Electrochem. And Solid-State Letters*, 13, pp. H290-H293; 2010.

[17] von Keudell, A., *Thin Sold Films*, 402, pp. 1-37; 2002.

[18] Grill, A., Patel, V., Jahnes, C., *J. Electrochem. Soc.*, 145, pp. 1649-1653; 1998.

[19] Vrtis, R.N., O'Neill, M.L., Vincent, J.L., Lukas, A.S., Peterson, B.K., Bitner, M.D., Karwacki, E.J., *Mater. Res. Soc. Symp. Proc.*, 766, pp. E.7.4.1-6; 2003.

[20] Strittmatter, R.J., Hahnfeld, J.L., Silvis, H.C., Stokich, T.M., Perry, J.D., Ouellette, K.B., Niu, Q.J., Godschalx, J.P., Kalantar, T.H., Mubarekyan, E., Hefner, Jr., R.E., Lyons, J.W., Dominowski, J.M., Buske, G.R., *Mater. Res. Soc. Symp. Proc.*, 766, pp. E.7.5.1-8; 2003.

[21] Chang, C.-C., Pan, F.-M., Chen, C.-W., *Microelectronic Engineering*, 86, pp. 2241-2246; 2009.

[22] Broussous, L., Puyrenier, W., Rebiscoul, D., Rouessac, V., Ayral, A., *Microelectronic Engineering*, 84, pp. 2600-2605; 2007.

[23] Engbrecht, E.R., Cilino, C.J., Junker, K.H., Sun, Y.M., White, J.M., Ekerdt, J.G., *Mater. Res. Soc. Symp. Proc.*, 766, pp. E.8.2.1-6; 2003.

[24] Engbrecht, E.R., Sun, Y.M., Junker, K.H., White, J.M., Ekerdt, J.G., *J. Vac. Sci. Technol. A*, 22, pp. 2152-2158; 2004.

[25] Engbrecht, E.R., Sun, Y.M., Junker, K.H., White, J.M., Ekerdt, J.G., *J. Vac. Sci. Technol. B*, 23, pp. 463-467; 2005.

[26] Tokuyama, S. Hara, M., Kabir, M., Watanabe, D., Kimura, C., Aoki, H., Sugino, T., *Japanese Journal of Applied Physics*, 47, pp. 2492-2495; 2008.

[27] Sugiyama, T., Tai, T., Sugino, T., *Applied Physics Letters*, 80, pp. 4214-4216; 2002.

Chapter 2: Sealing Ultra Low κ Porous Dielectrics with Thin Boron Carbo-Nitride Films

2.1. INTRODUCTION

The semiconductor industry continues to scale down device sizes on integrated circuits. This size scaling must be applied to all levels of the circuit, including the backend structures of the copper interconnect. Ever shrinking physical dimensions increase the resistive-capacitive (RC) delay of the electrical signal carried by the metal lines [1]. A possible solution to lowering the RC delay is the application of porous dielectric structures that incorporate air into the dielectric material, lowering the dielectric constant.

The integration of porous ultra low κ ($\kappa \leq 3$) materials into the process reveals a new set of design concerns. The introduction of pores into the dielectric lowers the mechanical strength of the material and allows for precursor penetration during further processing steps [2], such as chemical (or atomic layer) deposition of the copper diffusion barrier and metal seed layers. Precursor penetration is undesirable, as it causes a change in the physical properties of the dielectric, which may severely reduce device performance. Precursor penetration depth is dependent on the pore size and porosity of the dielectric as well as the chemistry of the deposition technique for the overlying film.

The present study examines a porous methyl silsesquioxane (PMSQ) ultra low κ (ULK) dielectric. In general the average pore size, pore size distribution, and pore interconnectivity of a MSQ are dependent on the porogen used [3], and these parameters change during plasma etching and subsequent ashing of the etch residue [4]. Any sealing strategy will have to adapt to a range of pore sizes and pore mouth openings that may differ considerably from the as-deposited dielectric film. For example, Kumar, *et al.*, reported a roughening and pore widening effect through a significant depth (165 nm) of a PMSQ-based dielectric due to C_4F_8 plasma etching [4]. The interconnected channels created during the plasma treatment were 5-8 nm wide, whereas they were likely 1.5-2 nm before plasma treatment.

Potential solutions to precursor penetration have involved either surface modification of the dielectric [5-8] or the deposition of an additive sealing layer [2,4,9-13]. Surface modification techniques involve an energy assisted process to densify the first few nanometers of the dielectric surface. Certain plasma treatments have proven to be effective in sealing pores. In plasma treating the surface, it is important to consider the competing ion bombarding and etching processes [6]. Conversely, the plasma etching chemistry commonly used in the formation of trenches in the dielectric was shown to increase surface roughness and chemically change the dielectric material [14]. Methods employed to seal the porous dielectric have involved both organic [2,9-11] and inorganic [4,12,13] films. A polymer liner as thin as 3.5 nm was able to seal the pores of a PMSQ and prevent copper diffusion [2]. Composite Ta/SiCN barriers were able to seal a porous organic spin-on dielectric at a combined thickness of 20 nm [12]. This paper reports studies employing amorphous boron carbo-nitride (BC_xN_y) films of varying thickness to seal etched and ashed PMSQ layers. The BC_xN_y seals the pores and pore openings within the first few nm of the porous material surface; an average thickness of several nm effectively seals the low κ dielectric from subsequent infiltration.

2.2. EXPERIMENTAL

Experiments were performed on blanket, etched and ashed PMSQ films deposited on a Si(100) wafer. BC_xN_y was also deposited on patterned PMSQ films, the dimensions of which were 175 nm across the dielectric and 125 nm wide × 310 nm deep trenches. Samples were cleaved from 200 mm wafers to a size of 2.2 × 2.2 cm. The unetched PMSQ has a pore size of maximum probability of 1.26 nm as determined by argon adsorption, and a pore size of maximum probability of 1.36 nm and pore average pore diameter of 1.91 nm as determined by nitrogen adsorption. Pore size distributions were not recorded after etching and ashing the PMSQ.

Measurement of a BC_xN_y film thickness directly on porous substrates is not possible due to the irregular, nonplanar nature of the BC_xN_y – ULK interface. Film thicknesses on the ULK substrates were estimated by first depositing control samples of BC_xN_y on thin (7.3 nm and 10.9 nm), thermally-grown SiO_2 on Si(100). The control thicknesses were determined by ellipsometry using a J.A. Woollam VASE^{TM} spectroscopic ellipsometer and also checked using Si 2p peak attenuation by x-ray photoelectron spectroscopy (XPS). The same deposition conditions were then immediately used to grow BC_xN_y on a porous ULK sample.

Film growth was carried out in a stainless steel chemical vapor deposition (CVD) reaction vessel. The samples were put into a load lock, pumped down to 1×10^{-7} Torr, and transferred via transfer arm to the reactor. This apparatus has been described elsewhere [15]. Samples were preheated for 30 min at 335 °C in 10 standard cubic centimeters per min (sccm) Ar at 1 Torr. BC_xN_y films were deposited using solid dimethylamine borane [$NH(CH_3)_2{:}BH_3$] and C_2H_4 coreactant gas. The dimethylamine borane precursor was heated to 41 °C in a stainless steel container and dosed to the reactor using 10 sccm Ar carrier gas. Ethylene was dosed to the reactor at 0.8 sccm. CVD occurred at 1 Torr total pressure and 335 °C. At these conditions, amorphous $BC_{0.9}N_{0.07}$ with κ ~3.7 is formed [15]. Deposition time was varied to obtain different film thicknesses, *e.g.*, a 5 nm film was deposited in 20 min. The sample was cooled for 15 min at 1 Torr in 10 sccm Ar, followed by further cooling at 1×10^{-7} Torr for 20 min.

After cooling in the CVD chamber, samples were transferred *in-situ* to a different deposition chamber. For blanket film studies, samples were preheated for 40 min at 230 °C and 1×10^{-7} Torr and exposed to TaF_5 vapor for 60 s followed by 10 min cooling under 10 sccm Ar. Solid TaF_5 precursor was held at 98 °C in a stainless steel vessel. For patterned PMSQ substrates, CVD $TaSi_x$ films were deposited on the BC_xN_y films using the same reactor conditions, adding Si_2H_6 as a coreactant gas delivered to the reactor at 20 sccm. The samples were further cooled under vacuum in the deposition chamber and transferred *in-situ* to an analysis chamber. A Physical Electronics 3057^{TM} XPS system, operated with 58.7 eV pass energy and Al Kα radiation at 250 W, was used to characterize the samples. An Ar^+ ion gun was used to sputter samples at 5 keV, 25 mA beam current, and a 3 mm × 3 mm raster area. Separate studies established the etch rates [16].

Additional *ex-situ* analyses were performed on both the blanket and patterned samples. Backside secondary ion mass spectrometry (SIMS) depth profiling of TaF_5/BC_xN_y/blanket PMSQ/Si samples was obtained using an ADEPT-1010 spectrometer. The sample was epoxied top surface down on a piece of glass. The Si was polished until <0.5 μm remained. The surface was bombarded with O_2^+ ions at an impact energy of 2 keV and incident angle of 45°. The resulting ions from the surface were monitored to determine film composition. The depth of the sputtered feature was determined by stylus profilometry. $TaSi_x/BC_xN_y$/patterned PMSQ/Si samples were prepared for transmission electron microscopy (TEM), electron energy loss spectroscopy

(EELS), and energy dispersive x-ray spectroscopy (EDXS) analyses. The trenches were filled with tetraethoxysilane and capped with SiN. Cross sectioning of the samples was done on a Gatan precision ion polishing system (PIPS^{TM}). EELS and EDXS data were recorded in scanning tunneling electron microscopy (STEM) mode while stepping small focused electron probes of ~3 Å and ~5 Å diameter, respectively, across a sidewall feature of the sample. EELS integration windows were from 142 to 144, 174 to 194, 315 to 320, 405 to 425, and 540 to 560 eV for silicon, boron, carbon, nitrogen, and oxygen, respectively. The EDXS integration window is from 8.1 to 9.7 keV for tantalum Lα.

2.3. RESULTS

A series of thermal CVD BC_xN_y films were deposited on 220-nm thick, blanket, etched and ashed PMSQ films on Si(100). The BC_xN_y film thicknesses ranged from 1.8 to 40.6 nm. After BC_xN_y deposition the film stacks were exposed to TaF_5. These experiments were carried out to determine the minimum thickness necessary to seal the porous substrate and prevent infiltration of a representative CVD/atomic layer deposition precursor that might be used to deposit the barrier/seed layer. XPS depth profiling was used as a first estimate for pore sealing success or failure. BC_xN_y was deposited on blanket SiO_2 and depth profiled to determine the sputtering rate; this sputtering rate was then used to approximate BC_xN_y – PMSQ interfaces [16]. A representative successful sealing result is shown in Fig. 2.1(a) for the TaF_5/6.3 nm BC_xN_y/PMSQ/Si stack structure. The B, C, N, O, Si, Ta, and F signals were monitored, and the C, F, N contributions are not shown. The Ta signal reaches negligible (<2 atom [at] %) concentrations before the calculated BC_xN_y – PMSQ interface (indicated by the dashed line).

Ex-situ backside SIMS was performed to determine if the residual Ta signal in the XPS depth profile (Fig. 2.1(a)) was due to precursor penetration or knock-in from Ar^+ ion sputtering. Figure 2.1(b) presents the backside SIMS results for the TaF_5/6.3 nm BC_xN_y/PMSQ/Si sample. C, N, O, Si, Ta, and F concentrations were followed through the substrate but only the C, Si, Ta contributions are shown. The rapid increase of the C signal near 180 nm indicates the location of the Si – PMSQ interface. There is no Ta signal until the O_2^+ ions sputter ~400 nm into the film stack from the back side. SIMS results from an unsealed PMSQ sample, which does not have any BC_xN_y grown on it, are shown in Fig. 2.2(b). The Ta SIMS signal appears along with the C signal at a sputtering depth of ~320 nm that corresponds to the Si – PMSQ interface location. This strong Ta signal persists throughout the PMSQ film. The XPS profile of an etched and ashed PMSQ film that does not have any BC_xN_y film on it is shown in Fig. 2.2(a) to illustrate a failed seal condition. In this TaF_5/PMSQ/Si sample, the Ta signal is significant at the surface (5 at %) and continues to rise throughout the film. The Si signal increases to 40 at % after 40 min of sputtering and this indicates the PMSQ – Si interface has been sampled. Even at this interface, the Ta signal is large (17 at %). Therefore, the residual (2 at %) Ta signal during the XPS depth profiling in Fig. 2.1(a) is attributed to a knock-in effect from the Ar+ ions used to physically sputter the surface. When Ta concentrations are found at the 2 % level, the BC_xN_y film is assumed to have sealed the pores.

By varying the BC_xN_y film thickness and monitoring the Ta signal in XPS depth profiling, the minimum thickness was found at which the PMSQ pores are sealed from precursor penetration. Figure 2.3(a) shows the XPS depth profile of a TaF_5/3.9 nm

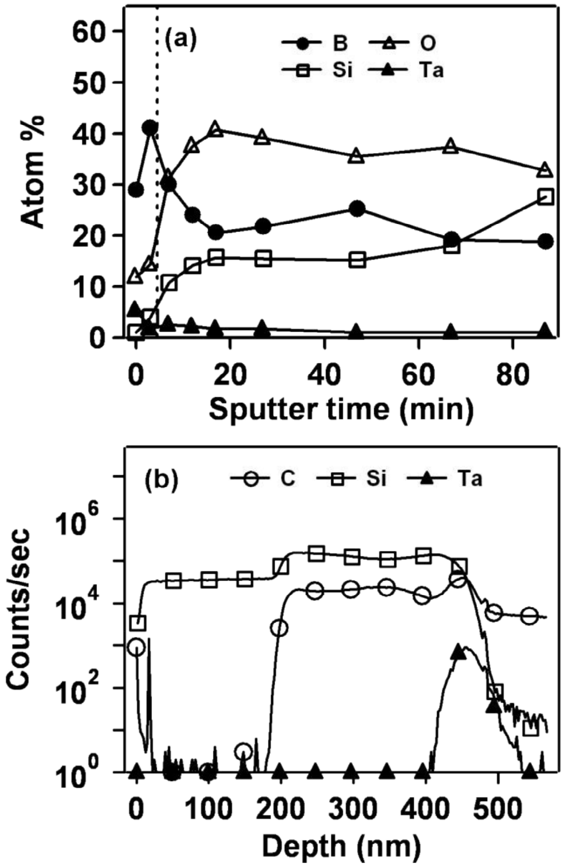

Figure 2.1. Depth profile of TaF_5/6.3 nm BC_xN_y/PMSQ/Si: (a) XPS analysis from the front side and (b) SIMS analysis from the backside. The dashed line indicates the estimated location of the BC_xN_y – PMSQ interface.

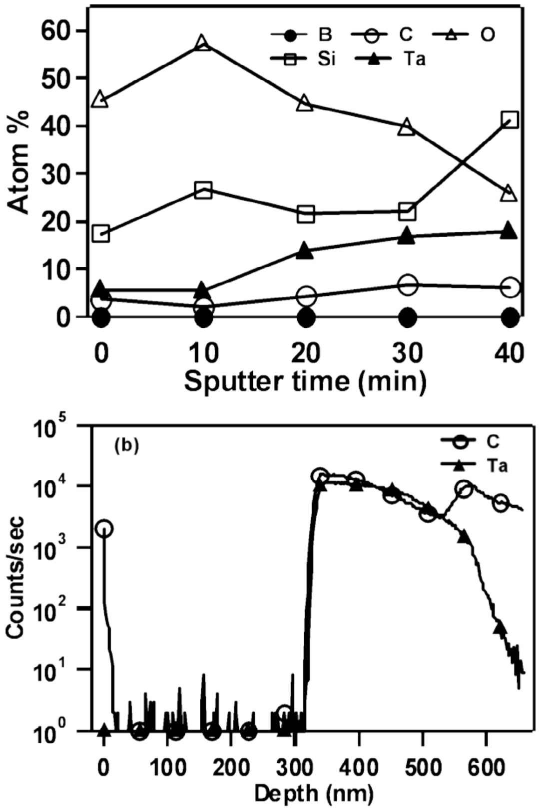

Figure 2.2. Depth profile of TaF_5/PMSQ/Si: (a) XPS analysis from the front side and (b) SIMS analysis from the backside.

BC_xN_y/PMSQ/Si sample. Here, only the B and Ta contributions are shown. The Ta signal attenuates to negligible values (<2 at %) past the interface. This sample was annealed for 40 min at 370 °C after the depth profiling and examined again. No change was observed in the depth profile, which suggests the BC_xN_y is thermally stable at this elevated temperature. Complementary backside SIMS was not done on this 3.9 nm BC_xN_y sample.

Figures 2.3(b) and 2.3(c) present the XPS profiles and SIMS profiles for a TaF_5/3.3 nm BC_xN_y/PMSQ/Si sample, respectively. This film stack represents a failed sealing condition. As with Fig. 2.2(b), the coincidence of the C and Ta signals near 220 nm shows that the TaF_5 precursor penetrated this sample during exposure to TaF_5 vapor for 60 s at 230 ºC. The Ta concentrations obtained by XPS depth profiling also show that TaF_5 vapor penetrated into the PMSQ region.

A patterned substrate is more representative of a dual damascene process structure, and experiments were performed on patterned PMSQ samples to more completely test the pore sealing ability of BC_xN_y films. Based on the blanket film results, BC_xN_y films at least 3.9 nm thick were targeted for study. After BC_xN_y deposition on the patterned samples, $TaSi_x$ films were deposited on the BC_xN_y. Figure 2.4(a) shows the STEM image of a sidewall structure for a sample with a 3.9 nm BC_xN_y film. The bright features on the sidewall are where $TaSi_x$ has nucleated. The line through the sidewall indicates where EELS/EDXS analysis (shown in Fig. 2.4(b)) was performed. The solid lines in Fig. 2.4(b) indicate the region where the BC_xN_y film resides and were determined by measuring across the line scan at points where contrast changed on the TEM image. The dotted line is an estimate of the approximate BC_xN_y – PMSQ interface location. This location is based on ellipsometry and Si 2p peak attenuation measurements of BC_xN_y

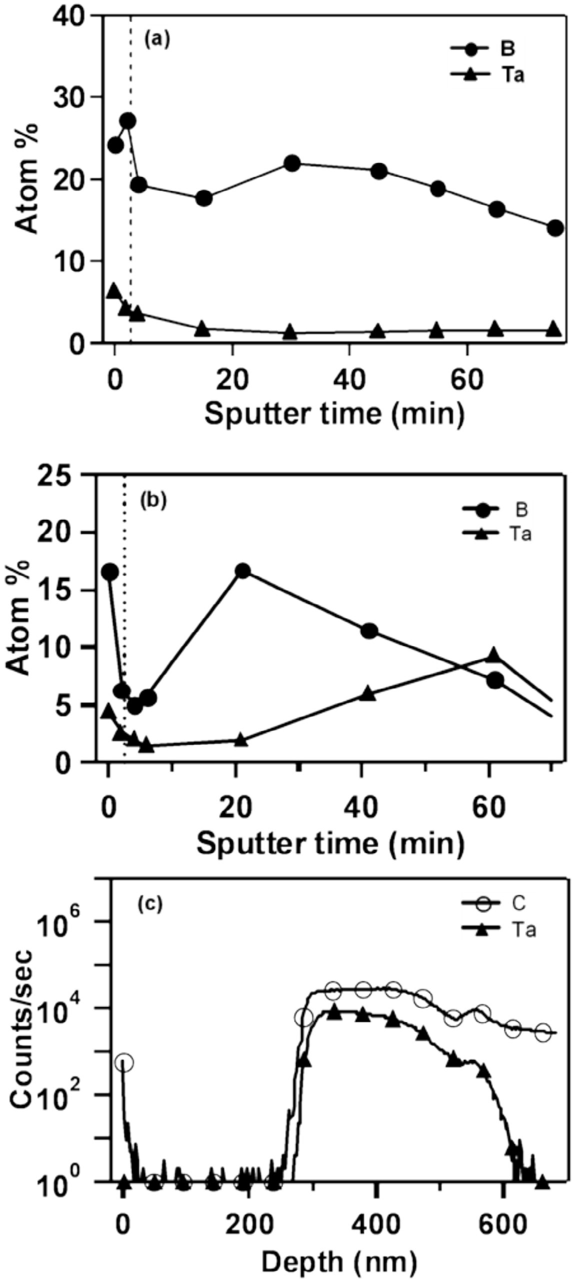

Figure 2.3. Depth profiles of: (a) TaF_5/3.9 nm BC_xN_y/PMSQ/Si using XPS analysis from the front side, (b) TaF_5/3.3 nm BC_xN_y/PMSQ/Si using XPS analysis from the front side, and (c) TaF_5/3.3 nm BC_xN_y/PMSQ/Si using SIMS analysis from backside. The dashed line indicates the estimated location of the BC_xN_y – PMSQ interface.

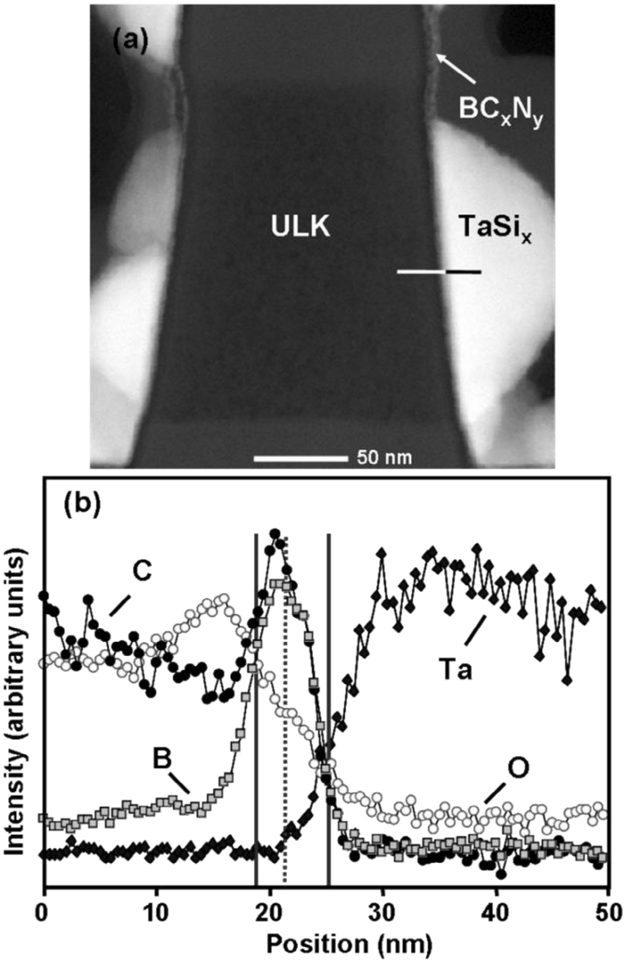

Figure 2.4. (a) HAADF-STEM image of a $TaSi_x$/3.9 nm BC_xN_y/PMSQ patterned sidewall structure and (b) the corresponding EELS/ EDXS analysis of the feature. The solid lines indicate the region where BC_xN_y is present, based on contrast change of the TEM image. The dotted line is an estimate of the approximate PMSQ – BC_xN_y interface relative to the BC_xN_y – $TaSi_x$ interface that is based on the 3.9 nm film thickness.

films that were deposited on blanket SiO_2 immediately before BC_xN_y deposition was done on the patterned substrates. Both the B and C EELS signals begin to rise at the beginning of the BC_xN_y – $TaSi_x$ interface (~25 nm). These signals peak at ~21 nm, then attenuate rapidly at the PMSQ – BC_xN_y interface. The C signal increases again, owing to the methyl groups in PMSQ. The B signal decreases to near the baseline level, but persists throughout the PMSQ region sampled. This is due to dimethylamine borane precursor penetration into the pores. An appreciable Ta EDXS signal is seen in the $TaSi_x$ region that decreases rapidly at the BC_xN_y – $TaSi_x$ interface. The Ta signal attenuates completely within the BC_xN_y layer.

A 5.1 nm BC_xN_y film on patterned PMSQ was also analyzed in this way. Figure 2.5 shows the TEM and EELS/EDXS results. On the left side of the TEM image (Fig. 2.5(a)), the entire trench is filled with $TaSi_x$. The same features that appear in the 3.9 nm BC_xN_y sample are also seen here. In this analysis, the left sidewall was scanned, therefore the scan originates in the $TaSi_x$ film (Fig. 2.5(b)). The Ta EDXS signal also attenuates completely within the BC_xN_y film.

2.4. DISCUSSION

The possible infiltration of TaF_5 into blanket, etched and ashed PMSQ that is capped with BC_xN_y was studied for a range BC_xN_y thicknesses. The experiments on blanket PMSQ resulted in an estimate for the BC_xN_y thickness (t) necessary to seal the pores. BC_xN_y films with $t < 3.3$ nm were unable to seal the pores, while films with $t \geq 3.9$ nm prevented TaF_5 penetration into the PMSQ. A residual XPS Ta 4*f* XPS signal, corresponding to less than 2 at %, was detected as a function of sputtering depth and this

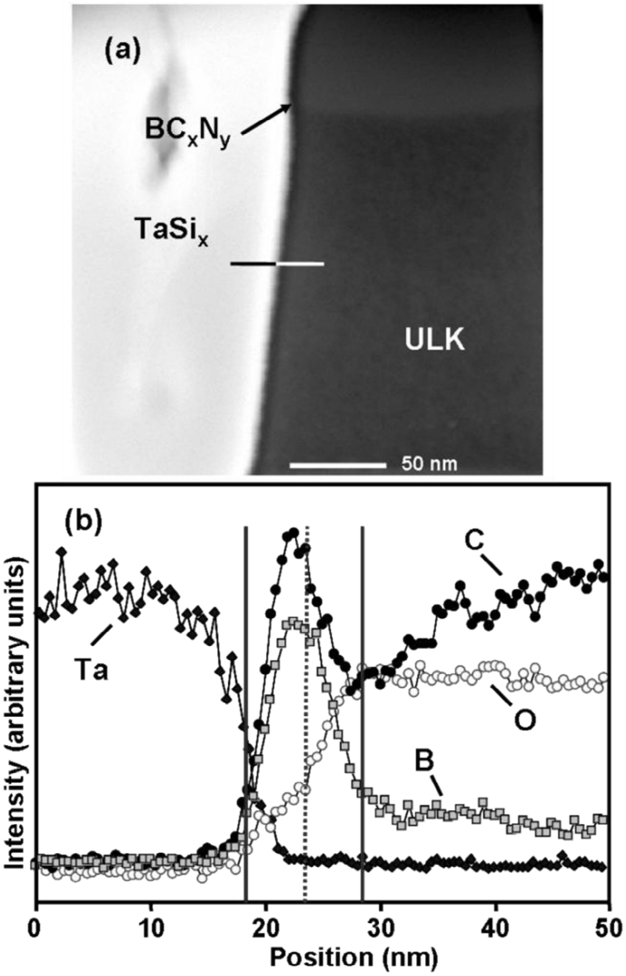

Figure 2.5. (a) HAADF-STEM image of a $TaSi_x$/5.1 nm BC_xN_y/PMSQ patterned sidewall structure and (b) the corresponding EELS/EDXS analysis of the feature. The solid lines indicate the region where BC_xN_y is present, based on contrast change of the TEM image. The dotted line is an estimate of the approximate BC_xN_y – PMSQ interface relative to the BC_xN_y – $TaSi_x$ interface that is based on the 5.1 nm film thickness.

signal persisted into the bulk of all blanket PMSQ films that had a BC_xN_y film greater than 3.9 nm. Backside SIMS showed that the Ta signal did not extend into the bulk of these capped PMSQ films. Thus it is believed that the residual Ta signal in the XPS depth profiles was due to an Ar^+ ion knock-in effect. This is shown for the TaF_5/6.3 nm BC_xN_y/PMSQ/Si sample (Fig. 2.1(b)).

The B signal is also observed to penetrate throughout the bulk of the PMSQ for blanket samples (Figs. 2.1(a), 2.3(a), and 2.3(b)) and patterned samples (Figs. 2.4 and 2.5). This is expected, as the dimethylamine borane precursor should penetrate the porous ULK during BC_xN_y deposition in the same way as the TaF_5 penetrates an unsealed sample. The effect of dimethylamine borane penetration on the effective κ value of the structure is not known and warrants further study. Recent studies have shown that BC_xN_y dielectric constants lower than 2.0 are possible with thermal or UV irradiation after deposition [17,18], so there may be a way to adjust the effective κ of a BC_xN_y-sealed porous low κ material.

The ultimate test of pore sealing ability for BC_xN_y on PMSQ was the deposition of $TaSi_x$ films on patterned substrates. EELS/EDXS analysis was performed on a horizontal linescan across the sidewall feature, as shown in the TEM images (Figs. 2.4 and 2.5). The solid lines indicate the region that BC_xN_y inhabits. The B and C signals peak in this section, which shows that this is indeed the BC_xN_y film. The Ta signal attenuates completely to background levels as the line scan leaves the BC_xN_y region. This behavior is observed for both the 3.9 and 5.1 nm thick BC_xN_y film stacks.

The EELS/EDXS results suggest the PMSQ – BC_xN_y interface is not abrupt. This can be seen by the tailing off of the B EELS signals into the PMSQ region of the stacks. This is most clearly illustrated in Fig. 2.5. Because the average pre-etched PMSQ pore size is small (1.9 nm), it is doubtful that during BC_xN_y CVD deposition a film of BC_xN_y

completely lines the pore walls throughout the entire interconnected pore network. The authors believe instead that there are nucleation events near the interior of the pore mouths that eventually pinch off the bulk pore void volume as suggested by Illustration 2.1. The smaller pores will close up at a thinner BC_xN_y capping film thickness than will be required to seal the larger pores. It is not necessary that this pinching off occurs at the mouth where the pores meet the free surface. Cho, *et al.*, found that the pore neck size, or interconnection radius was the most important factor in determining the time required to seal a porous substrate [19]. Therefore, a small neck interconnecting pores near the free surface could also serve as the sealing site. The distribution of pores present in the unetched PMSQ will produce a diffuse interface with differing extents of BC_xN_y penetration away from the growth surface. Etching is expected to amplify the pore size distribution near the surface [4], which will likely serve to make the interface more diffuse.

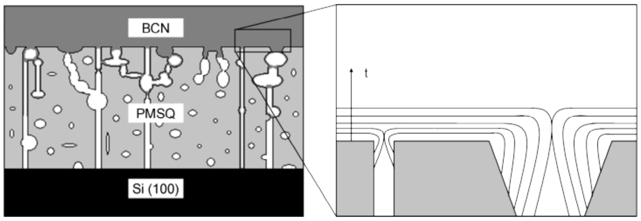

Illustration 2.1. Representation of the cross section of the stacked structures studied by EELS/EDXS. A closer view of the BC_xN_y – PMSQ interface at two of the pore mouths illustrating the possible growth of the BC_xN_y that leads to a pinching off of a pore. The thickness arrow, *t*, indicates the direction of capping film growth with increased deposition time.

2.5. SUMMARY

BC_xN_y films of varying thickness were deposited on blanket and patterned PMSQ substrates. Blanket film samples were then exposed to TaF_5 and analyzed by XPS and SIMS depth profiling. $TaSi_x$ films were grown on patterned samples and Ta profiles across the patterned samples were analyzed by EDXS. The minimum BC_xN_y capping-layer thicknesses required to seal pores was 3.9 nm on both blanket and patterned PMSQ substrates.

2.6. REFERENCES

[1] Cunningham, J., *Semiconductor International*, April 2000, pp. 1-8; 2000.

[2] Jezewski, C., Wiegand, C.J., Ye, D., Mallikarjunan, A., Liu, D., Jin, C., Lanford, W. A., Wang, C., Senkevich, J.J., Lu, T.-M., *J. Electrochem. Soc.*, 151; pp. F157-F161; 2004.

[3] Xu, J., Moxom, J., Yang, S., Suzuki, R., Ohdaira, T., *Appl. Surf. Science*, 194, pp. 189-194; 2002.

[4] Kumar, R., Wong, T.K.S., Murthy, B.R., Wang, Y.H., Balasubramanian, N., *J. Electrochem. Soc.*, 153, pp. G420-G427; 2006.

[5] Travaly, Y., Schuhmacher, J., Baklanov, M.R., Giangrandi, S., Richard, O., Brijs, B., Van Hove, M., Maex, K., Abell, T., Somers, K.R.F., Hendrickx, M.F.A., Vanquickenborne, L.G., Ceulemans, A., Jonas, A.M., *J. Appl. Phys.*, 98, pp. 083515-1-9; 2005.

[6] Hoyas, A.M., Schuhmacher, J., Whelan, C.M., Baklanov, M.R., Carbonell, L., Celis, J.P., Maex, K., *J. Vac. Sci. Technol. B*, 23, pp. 1551-1557; 2005.

[7] Mannaert, G., Baklanov, M.R., Le, Q.T., Travaly, Y., Boullart, W., Vanhaelemeersch, Jonas, A.M., *J. Vac. Sci. Technol. B*, 23, pp. 2198-2202;2005.

[8] Patel, Z.P., Roy, A.N.U., Bakhru, H., Lu, T.-M., *Thin Solid Films*, 476, pp. 322-325; 2005.

[9] Juneja, J.S., Ten Eyck, G.A., *J. Vac. Sci. Technol. B*, 23, pp. 2232-2235; 2005.

[10] Carrow, B.P., Murray, R.E., Woods, B.W., Senkevich, J.J., *Mater. Res. Soc. Symp. Proc.*, 863, pp. B2.10.1-6 ; 2005.

[11] Senkevich, J.J., Jezewski, C., Lu, D., Lanford, W.A., Wang, G.-C., Lu, T.-M., *Mater. Res. Soc. Symp. Proc.*, 812, pp. F1.21-10; 2004.

[12] Chen, X.T., Gui, D., Chi, D.Z., Wang, W.D., Babu, N., Hwang, N., Lo, G.Q., Kumar, R., Balasubramanian, N., Kwong, D.-L., *IEEE Electron. Device Lett.*, 26, pp. 616-618; 2005.

[13] Chen, Z., Prasad, K., Li, C.Y., Lu, P.W., Su, S.S., Tang, L.J., Gui, D., Balakumar, S., Shu, R., Kumar, R., *Appl. Phys. Lett.*, 84, pp. 2442-2444; 2004.

[14] Lazzeri, P., Hua, X., Oehrlein, G., Barozzi, M., Iacob, E., Anderle, M. *J. Vac. Sci. Technol. B*, 23, pp. 1491-1498; 2005.

[15] Engbrecht, E.R., Sun, Y.-M., Junker, K.H., White, J.M., Ekerdt, J.G., *J. Vac. Sci. Technol. A*, 22, pp. 2152-2158; 2004.

[16] Fitzpatrick, P.R., Satyanarayana, S., Sun, Y.-M., White, J.M., Ekerdt, J.G., *Mater. Res. Soc. Symp. Proc.*, 863, pp. B6.8.1-6; 2005.

[17] Sugino, T., Tai, T., Etou, Y., *Diamond Relat. Mater.*, 10, pp. 1375-1379; 2001.

[18] Tai, T., Sugiyama, T., Sugino, T., *Diamond Relat. Mater.*, 12, pp. 1117-1121; 2003.

[19] Cho, W., Saxena, R., Roderiguez, O., Ojha, M., Achanta, R., Plawsky, J.L., Gill, W.N., *J. Electrochem. Soc.*, 152, pp. F61-F65; 2005.

Chapter 3: Bonding Characteristics of BC_xN_y: Variation of H Content with Growth Temperature and Annealing

3.1. INTRODUCTION

Boron carbo-nitride (BC_xN_y, referred to herein as BCN for simplicity) is a candidate material for use as a copper diffusion barrier and pore sealing liner material. BCN films deposited by a single source precursor as well as with coreactant gases have been tested as a copper diffusion barrier in metal insulator semiconductor capacitor structures by time dependent dielectric breakdown (TDDB) tests. The C_2H_4 coreactant films performed the best compared to a commercial $SiC_{0.76}N_{0.44}$ film [1]. BCN films deposited at a growth temperature of 335 °C using dimethylamine borane (DMAB) vapor and C_2H_4 coreactant on blanket etched and ashed porous methylsilsesquioxane low κ material was found to be effective at preventing TaF_5 precursor from penetrating into the porous material with films as thin as 3.9 nm [2].

One of the most important requirements of a barrier/liner material is that it must behave well electrically. This means that the material must be a good insulator, and must be resistant to charge transfer. The main methods used to test dielectric materials electrically are by capacitance-voltage and current-voltage measurements. Fitzpatrick studied the electrical performance of C_2H_4 and NH_3 coreacted BCN films in MIS capacitor structures on Si(100). The C_2H_4 coreacted films displayed a large flatband voltage shift, and the magnitude of this shift increased with increasing BCN film thickness. Additionally, a large hysteresis was observed in the CV behavior when sweeping from negative to positive gate voltage and reverse. Films coreacted using NH_3 displayed less flatband shift and less CV stretch for BCN grown at lower substrate temperature. Leakage current was also lower for films deposited at lower growth temperature [3].

The flatband voltage shift of a MIS device is dependent on the metal semiconductor work function along with the various charges located in the bulk of the insulator and at the insulator-semiconductor interface. The polarity of the voltage shift seen in C-rich BCN films suggests the existence of fixed negative charge, which could be due to the increased amount of C in these films, some of which may be sp^2 hybridized. XPS deconvolution of the C 1*s* peak is not possible for determining C hybridization due to the small energy shift between the sp^2 and sp^3 states. A continuum of states may exist in amorphous C -containing structures rather than pure sp^2 and sp^3 configurations [4]. The increased fixed charging seen in N-rich films deposited at higher growth temperatures may also be due to unsatisfied bonds. Hydrogen readily satisfies dangling bonds. A potential measure of bond saturation lies in quantifying the H-bonding in these films.

Another important requirement for an insulating barrier is having the lowest κ possible, thereby minimizing the overall capacitance of the interconnect, reducing RC delay. By changing the deposition temperature and coreactant gas of the CVD process, BCN films have been deposited with varying dielectric constant ($3.7 < \kappa < 4.6$) [5]. Sugino, *et al.*, deposited hexagonal polycrystalline BCN by plasma assisted CVD with κ as low as 2.4 and this was reduced further to 1.9 with a 15 minute anneal at 400 °C [6]. It was suggested that the mechanism for this change in κ is due to a reduction in C-H and C=C bonding, as measured by FTIR [7]. A number of studies reported decreased dielectric constants and associated changes in the optical constants of PECVD deposited SiCOH films after post deposition anneals. The reduction in κ is linked to removal of volatile CH_x species from the films [8-10].

The research presented here characterizes the physical differences between ethylene codeposited films and ammonia codeposited films. The various chemical bonding states of these films are studied as a function of growth temperature between 300 and 400 °C. To probe the variations in H-bonding with choice of coreactant gas and growth temperature, SIMS and FTIR are employed. The FTIR bonding information is also coupled with the XPS binding state information to give a more complete picture of the BCN system. The valence band offset of the BCN/Si heterojunction is measured by high resolution XPS to determine if the energy barrier to electron transport is due to an interfacial layer or from the bulk film characteristics. High temperature anneals in forming gas are carried out on all samples and XPS and ellipsometry are employed to observe how the properties of these films change under different annealing temperatures.

3.2. EXPERIMENTAL

BCN films were deposited on 2.2 × 2.2 cm^2 coupons cleaved from Si(100) n-type wafers. Prior to film growth the substrates were cleaned by sonicating in acetone for 5 min and rinsed with ethanol and de-ionized (DI) water. For the XPS deconvolution studies, this was the only precleaning step. Samples prepared for FTIR study and valence band offset measurements were etched for 20 min in piranha solution (H_2SO_4:H_2O_2:H_2O = 6:2:1), etched for 40s in 1% HF solution, and rinsed for 1 min in DI water to ensure a clean interface. The annealing study samples were subjected to the HF etching step to remove the native oxide layer but were not piranha cleaned.

Immediately after cleaning the samples were blown dry with He, loaded into a vacuum chamber, pumped down in a load lock, and transferred to a CVD chamber. Samples were preheated for 30 min at temperatures from 300-400 °C at 1 Torr in 10

SCCM Ar to the desired growth temperature. All BCN films were deposited at 1 Torr. Pressure was held constant by pumping on the chamber with a mechanical pump and by use of a variable position butterfly valve and a baratron pressure gauge in the chamber. Depositions were performed using solid dimethylamine borane [$NH(CH_3)_2:BH_3$] (DMAB) heated in a stainless steel bubbler to 43°C. The vapor pressure of DMAB at 43°C is ~356 mTorr [11]. Ar was flowed through the bubbler at 10 SCCM (SCCM denotes standard cubic centimeters per minute at STP) as a carrier gas for the DMAB vapor. Either C_2H_4, at 0.8 SCCM, or NH_3, at 10 SCCM, was used as a coreactant gas to produce carbon rich (C-rich) and nitrogen rich (N-rich) films, respectively. After deposition, the chamber was evacuated and samples were cooled in vacuum for 30 min and either transferred to the XPS analysis chamber or removed from the vacuum system.

Samples were analyzed by XPS in a chamber held at a base pressure of 5×10^{-9} Torr. XPS measurements were taken with a Physical Electronics 5500^{TM} system using the Al anode and 56.7 eV pass energy. Films analyzed *in situ* were sputtered with Ar^+ ions from an ion gun for 2 min to remove adventitious carbon before XPS analysis. Here, the sputtering conditions were set at a voltage of 2 kV, current of 5 mA, pressure of 5 mPa, and the raster size was 3 mm × 3mm. The film composition was calculated using the atomic sensitivity factors for incident X-rays at 54.7° to the analyzer [12].

PeakFit^{TM} software was used to deconvolute the B 1*s*, C 1*s*, and N 1*s* spectra into their constituent bonding peaks. The C 1*s* and N 1*s* spectra were background subtracted using a linear function, while the B 1*s* data were prepared using a Shirley background subtraction. The peaks were fit using a combined Gaussian-Lorentzian sum function. The full width half maximum (FWHM) of the peaks were fixed using the following reference samples: PVD TaC_x for C 1*s* (1.8 eV), BN for B 1*s* (2.1 eV) and N 1*s* (1.8 eV) [5].

A series of samples deposited at conditions identical to those of the XPS analyzed samples was analyzed by FTIR. A Nicolet FTIR spectrometer equipped with a Harrick Scientific Products Ge crystal attachment allowed for attenuated total reflectance measurement of the BCN films. The analysis volume was purged with Ar beforehand to minimize absorbance from water. The spectrum was collected from 400-4000 cm^{-1} at a resolution of 2 cm^{-1}. Each spectrum was background subtracted with a reference bare Si(100) spectrum.

SIMS studies were performed using a Cameca SC Ultra instrument. The data was collected in dynamic mode. The surface was bombarded with a beam of Cs^+ ions at a voltage of 2 kV and a current of 1.7 mA. The beam incidence angle was 47.1°, and the data was collected in dynamic mode. The detected species in the analysis were negatively charged (M^-) secondary ions ejected from the surface during sputtering.

Valence band offset (VBO) measurements were taken by XPS analysis of samples using the Mg anode for superior resolution. The step size was set to 0.05 eV and 650 ms time/step. Each valence band spectrum was recorded from +15 eV to -5 eV, and the scan was repeated 100 times and averaged over all scans for increased signal/noise ratio.

High temperature anneals were done on samples that had been removed from vacuum and exposed to ambient. Annealing was performed in a tube furnace with a calibrated thermocouple attached behind the heating coils. The furnace was pumped down to a base pressure of 5×10^{-2} Torr. A forming gas mixture of 10% H_2, balance N_2 was flowed into the furnace at a rate of 10 SCCM and the pressure during annealing was held at 500 mTorr. The temperature was ramped at a rate of 10 °C/min and then held at a setpoint between 400-800 °C for 30 min. The furnace was cooled to below 100 °C in forming gas before the samples were removed.

BCN film thickness was measured using a two parameter Cauchy model on spectroscopic ellipsometry results collected at 65° and 70° relative to normal in the 500-1000 nm range on a JA Woolam VASE^{TM} instrument. The index of refraction, n, was determined by fitting the data using fixed film thickness and Cauchy parameters determined from the model fit.

3.3. RESULTS

3.3.1. BCN Bonding and Growth Temperature

3.3.1.1. XPS Analysis

The chemical composition and bonding states of the BCN films were studied by XPS. In the compositional analysis, the contribution from O 1*s* was not included. The amount of surface O was below 3% for all films and is attributed to surface contamination. Figure 3.1(a) depicts the atomic composition of N-rich BCN as a function of growth temperature. The overall amount of B decreases from 66 to 62% as growth temperature increases. At the same time, the N content increases from 25 to 29%. The atomic % of C stays fairly constant, below 9% throughout the temperature range.

Figure 3.1(b) shows the atomic composition of C-rich BCN as a function of growth temperature. Here, the atomic composition varies more drastically from 300-400 °C. The B content increases from 50 to 57% as growth temperature increases. C decreases from 47 to 35%. Like the N-rich samples, nitrogen increases with increasing

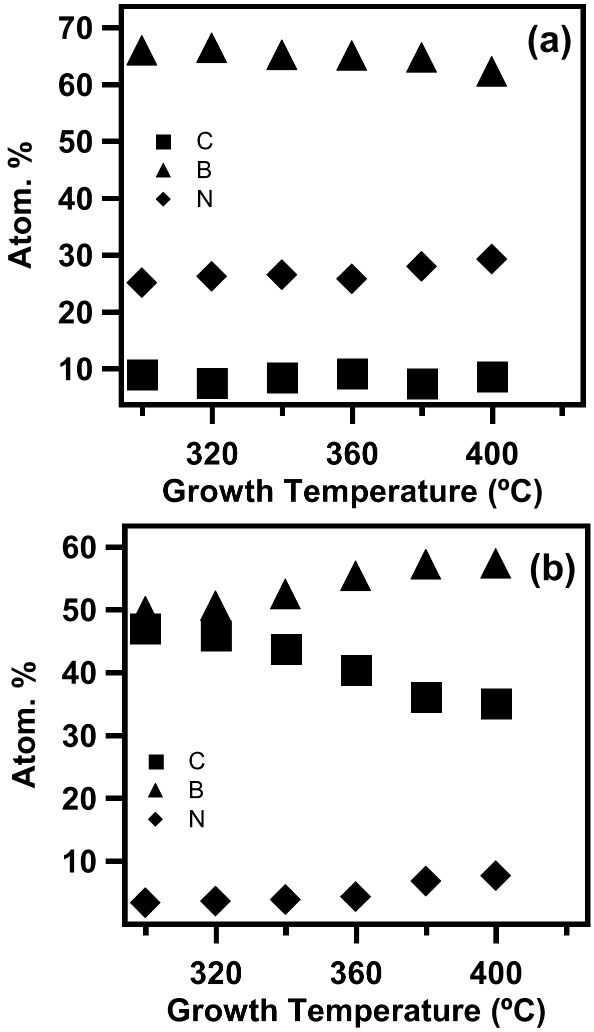

Figure 3.1. Atomic compositions calculated from XPS peak areas and atomic sensitivity factors for (a) N-rich and (b) C-rich BCN films grown at temperatures from 300-400 °C. The O 1*s* contribution was omitted from these compositions.

growth temperature. From these plots it is clear that the film composition for both N-rich and C-rich films is variable over the process temperature window.

Engbrecht found that BCN films deposited by DMAB alone exhibited a decrease in B content from 360 to 500 °C [11]. The amount of C increased roughly the same amount as B decreased up to 420 °C. The N-rich films that were deposited reflect the same B trend as those films deposited solely by DMAB. However the C content does not increase. Rather the N content increases. This may be due to the coreactant NH_3. NH_3 may bind more tightly to the surface than methyl groups, or it may react with dissociated intermediates of DMAB on the surface of sample. In fact, Engbrecht demonstrated that films deposited using NH_3 as a coreactant with DMAB compared to BCN deposited by DMAB alone had roughly half as much C and roughly double the N [12]. Unlike films deposited by DMAB alone, the C_2H_4 coreacted films display a marked decrease in C content, suggesting that C_2H_4 and its related dissociation products may not readily incorporate into the film at higher growth temperature.

The relative contribution of specific bonding states were determined by peak deconvolution. To aid in the discussion about the bonding states it is important to mention peak assignment. The peak fitting was performed by holding the FWHM of each subpeak constant, as chosen by reference values [5,12]. During the fitting procedure the centroids of the peaks were allowed to float to achieve the best fitting. The resulting positions of the peaks occur over a range of values. This is an expected result, as the bonding within the film changes as a function of temperature. Literature values of constituent bonding vary over a wide range of eV. C-N sp^3 bonding has been reported from 285.7-287.7 eV. C=N bonding has been reported from 285.3-287.7 eV [13,14]. The graphitic carbon peak is located at 284.5 eV, and B_4C is located at 283 eV [14]. Mixtures of BC_x are reported with B 1*s* at 188.4 eV and 189.4 eV for B_4C and $BC_{3.4}$, respectively

[15]. The peak position of B 1s owing to B-N has been assigned to 191.0 eV for h-BN [15]. N-B and N-C bonding in N 1s is reported at 398.4 eV and 398.4-400 eV [16].

Noting that these films are amorphous, and possibly consist of a number of combined bonding states involving B, C, and N, the peak assignments are made by expected position based on the electronegativity of the bond. This leads to domains of bonding where the peak assignment signifies the probable bond contribution as it appears in a network of other bonds. In general, all constituent peaks are shifted slightly higher in BE in the N-rich samples compared to the corresponding peaks in the C-rich samples, owing to the increased amount of more electronegative N. Figures 3.2 and 3.3 show the raw and fitted data for (a) 300 °C, (b) 360 °C, and (c) 400 °C deposited N-rich and C-rich films, respectively. The relative contributions to specific bonding states were extracted from this data and plotted as a function of temperature in the following figures.

Figure 3.4 shows the deconvoluted C 1*s*, B 1*s*, and N 1*s* data of films grown at various deposition temperatures for the N-rich BCN films. For the C 1*s* data (Fig. 3.4(a)), there appears a local minimum of C-B and a local maximum of C-N at around 350 °C. N-B and N-C bonding (Fig. 3.4(b)) only comprise about 70% of the total peak area. Between 30-35% of the relative bonding is found in another peak centered near 399.3 eV. This peak is attributed to a combined B-N-C bond, as the peak centroid lies between that expected for N-B and N-C bonding. The constituent B 1*s* bonding (Fig. 3.4(c)) exhibits the strongest linear dependence on temperature. B-B bonding decreases from 37 to 28 % of the total area as temperature increases. B-N bonding contribution increases from 20 to 26%. B-C bonding remains relatively stable at ~ 45%. This behavior is supported by the overall atomic composition change. The changes in constituent bonding for C 1*s* and

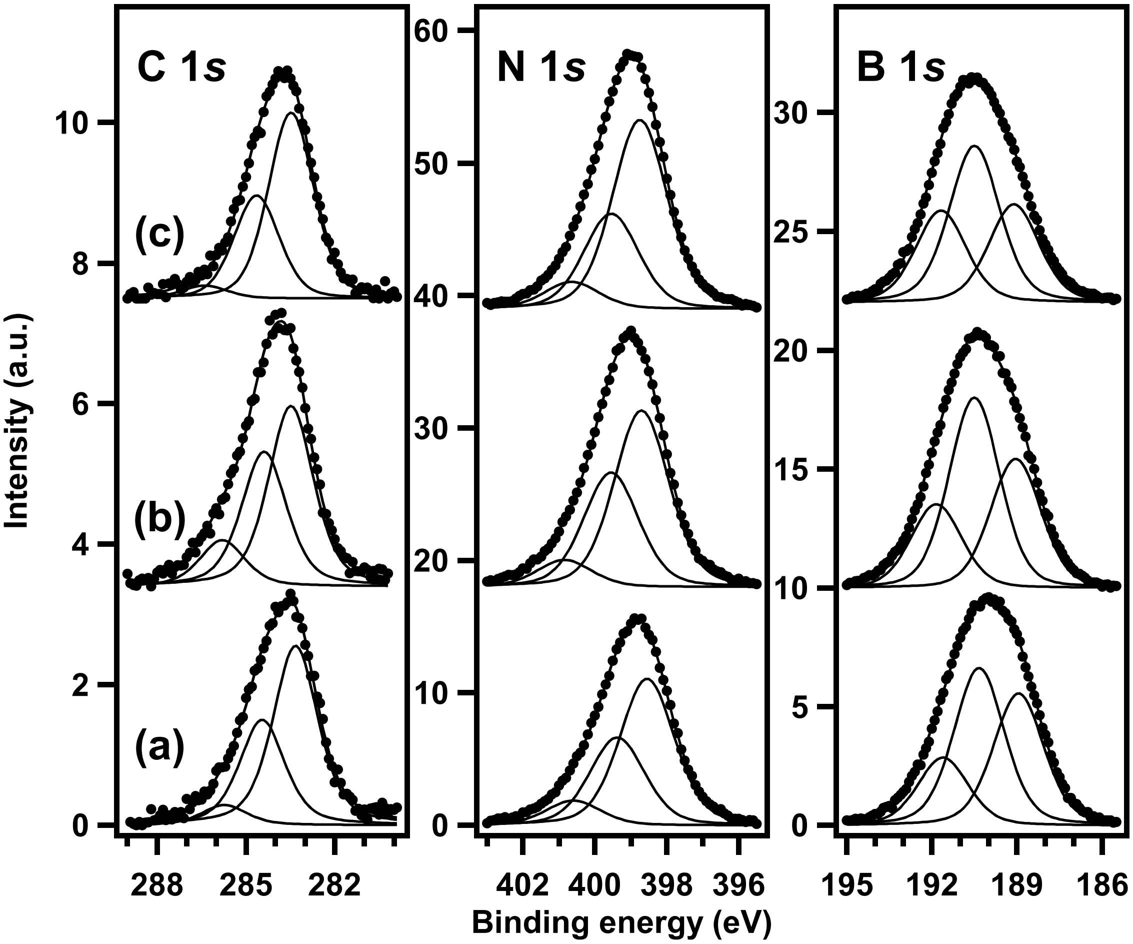

Figure 3.2. XP spectra of B 1*s*, N 1*s*, and C 1*s* regions of films deposited on Si(100) using DMAB and NH_3 at varying substrate temperatures of (a) 300 °C, (b) 360 °C, and (c) 400 °C. Individual peak contributions (solid lines) are fitted to the raw data (markers).

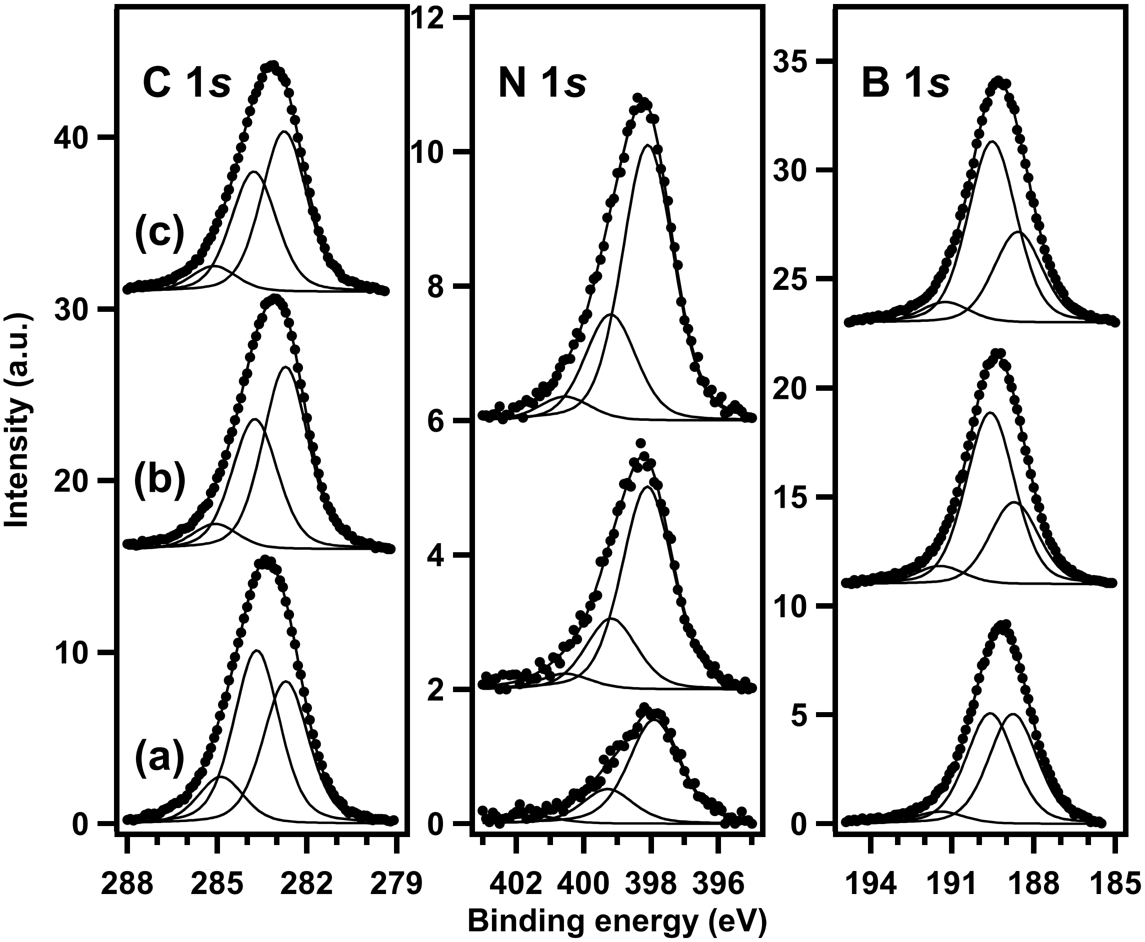

Figure 3.3. XP spectra of B 1*s*, N 1*s*, and C 1*s* regions of films deposited on Si(100) using DMAB and C_2H_4 at varying substrate temperatures of (a) 300 °C, (b) 360 °C, and (c) 400 °C. Individual peak contributions (solid lines) are fitted to the raw data (markers).

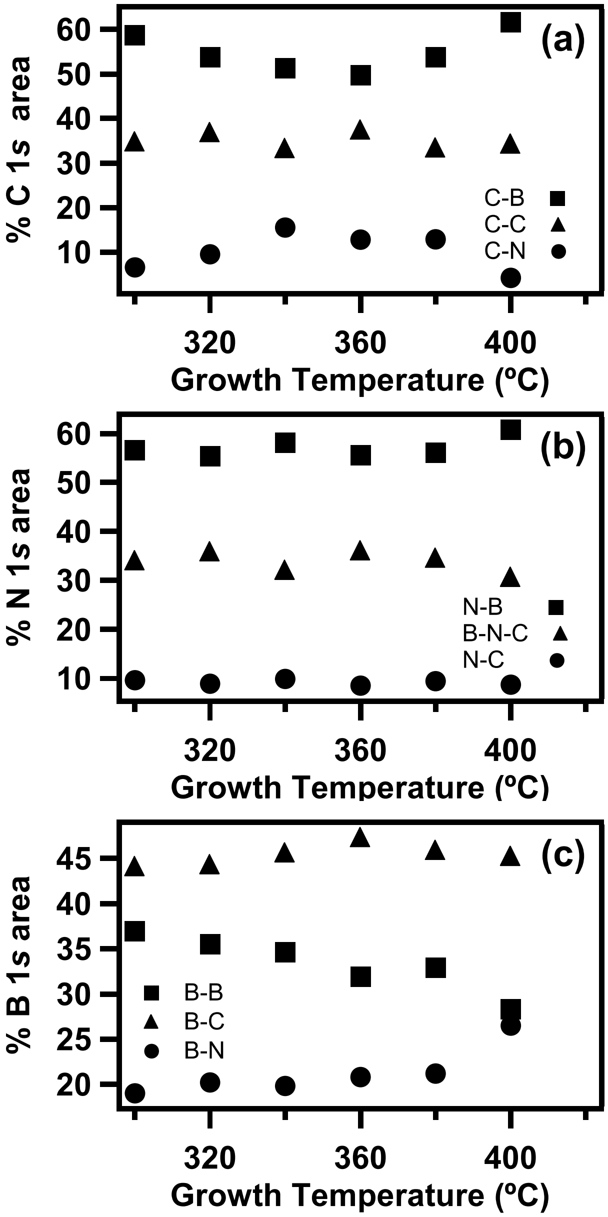

Figure 3.4. Deconvoluted contributions of (a) C 1*s* (b) N 1*s* and (c) B 1*s* XP spectra of N-rich BCN films deposited from 300-400 °C.

N 1*s* for the N-rich films may not trend as strongly with temperature because the overall films are composed less of these elements.

Figure 3.5 shows the deconvoluted C 1*s*, B 1*s*, and N 1*s* data over the temperature processing window, for the C-rich BCN films. For the C 1*s* deconvoluted peaks (Fig. 3.5(a)), the contribution from C-B bonding shifts from 40 to 50% from 300 to 320 °C, at the expense of C-C and C-N bonding. C-B bonding continues to increase to 380 °C while C-C bonding decreases. The B 1*s* constituent bonding (Fig. 3.5(c))reflects this change. B-C bonding increases from 47 to 60% of the total area while B-B bonding decreases from 47 to 30% up to 360 °C. Above this temperature these relative bonding contributions remain constant. Relative B-N bonding stays roughly the same over the temperature window, increasing slightly. N-B bonding decreases with increasing temperature while N-C peak contribution increases, as seen in Fig. 3.5(b). Recall that the overall composition of these C-rich films is enriched in B and slightly in N at the expense of C, for films deposited at higher substrate temperature. Therefore while the overall composition is increasing in B, the B is increasingly bound to C in the films.

3.3.1.2. FTIR Analysis

Figure 3.6 is a full FTIR spectrum for a C-rich film and an N-rich film. The full set of both C-rich and N-rich BCN films was analyzed with FTIR. These films were deposited at 340 °C and are representative of the entire set of collected data. There is no absorbance detected until 700 cm^{-1}. The first feature from 750-830 cm^{-1} is possibly due to B lattice vibrations [17]. The large, broad features ending at ~1490 and ~1570 for the C-rich and N-rich films, respectively, arise from the various B, N, and C bonding within the films. There is a small absorbance feature across 1570-1750 cm^{-1} for both types of films,

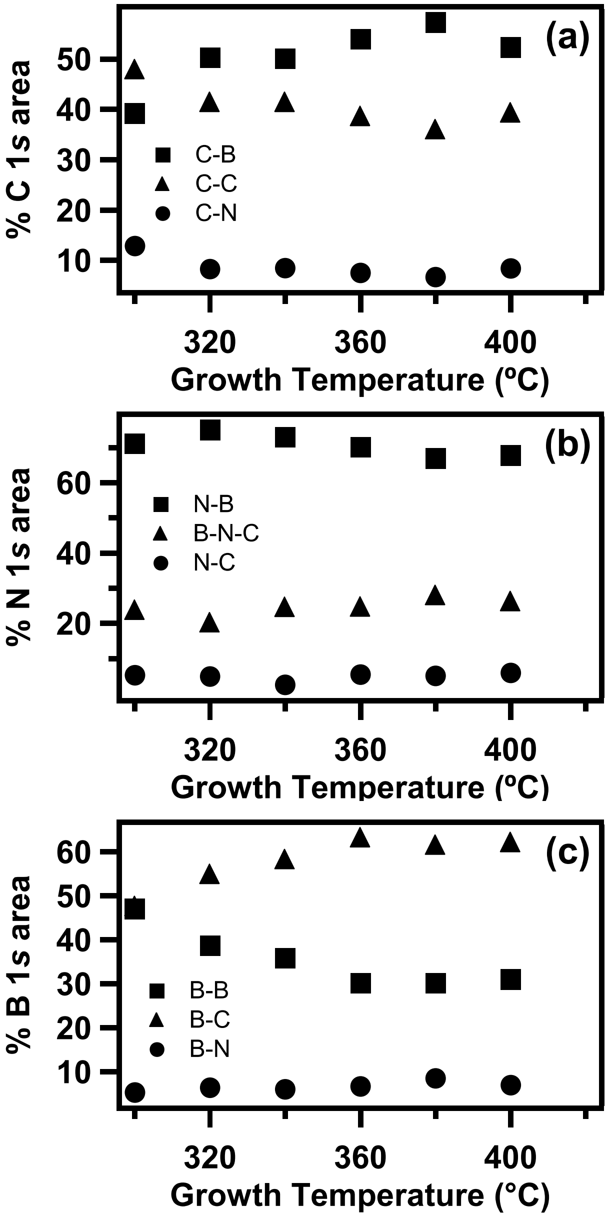

Figure 3.5. Deconvoluted contributions of (a) C 1*s* (b) N 1*s* and (c) B 1*s* XP spectra of C-rich BCN films deposited from 300-400 °C.

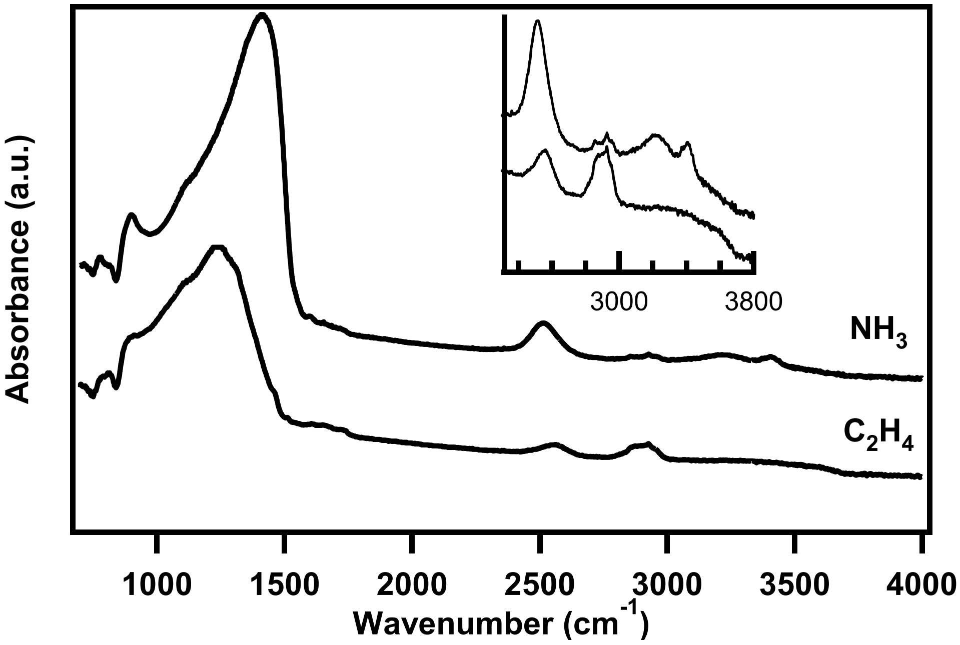

Figure 3.6. Full ATR FTIR spectra of N-rich (NH_3) and C-rich (C_2H_4) BCN films deposited on Si(100) at 340 °C. The inset provides a clear view of the peaks present from 2400-3800 cm^{-1}. These features are associated with –H stretching vibrations.

which may be due to deformation frequencies of primary and secondary amines [18,19] and the B-O stretching vibration in B-OH [17]. The various –H stretching modes are observed in bands from 2400-2700 cm^{-1}, 2800-3000 cm^{-1}, and from 3100-3600 cm^{-1}. This region is more clearly shown in the inset of Fig. 3.6. These modes are attributed to B-H stretching [13,20-23], C-H stretching [18,19,24-26], and either N-H or O-H stretching modes, respectively [13,17-19,27]. It is clear that for the N-rich film the broad feature is shifted to higher wavenumbers than that of the C-rich film. This indicates more N type bonding within the film. This was a common feature for all N-rich films. Another major difference between the two films was the relative intensity of the different –H stretching modes. In general, the C-rich films featured a more intense absorbance peak from the C-H stretching modes, and exhibited weaker B-H and N-H/O-H stretching absorbance peaks. B-H-B bridging bond absorbance [20] has been reported in amorphous hydrogenated boron films. Absorbance from nitrile groups has been reported in amorphous CN films deposited by RF sputtering [28] and ion beam assisted sputtering [29]. No absorbance features were observed for these BCN films between 1800-2400 cm^{-1}, suggesting that these absorbance modes are not present in these films or the absorbance cross sections are too weak to detect.

The main FTIR absorbance peaks of the BCN films contain contributions from many different IR active modes. The C-rich films have features at 1035, 1105, 1170, 1240, 1310, and 1385 cm^{-1}, as seen in Fig. 3.7. The feature at 1035 has been associated with the B-O-C stretching vibration [27]. While the amount of oxygen detected by XPS is negligible, these films have been shown to incorporate oxygen upon exposure to ambient [30], so it is not surprising to see O inclusive IR active stretching modes. The range of wavenumbers from 1000-1100 cm^{-1} is assigned to the spectrum of B-B to B-C bonding

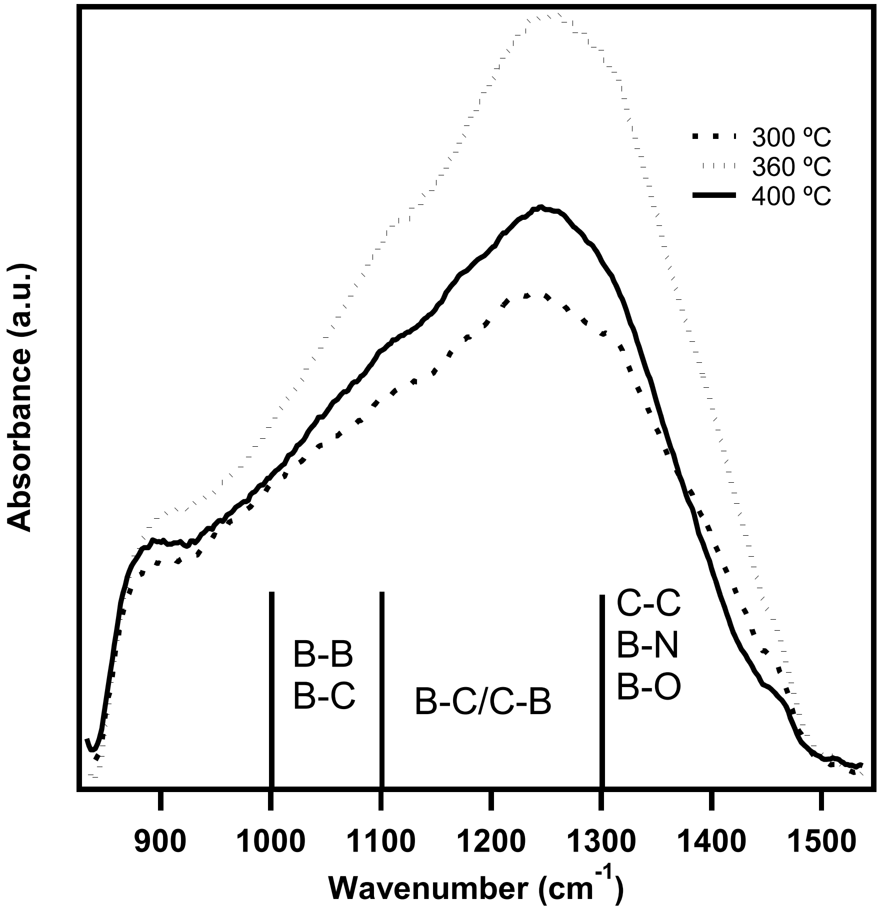

Figure 3.7. FTIR main peak absorbance region for C-rich BCN films deposited from 300-400 °C. The assigned bonding regions are labeled and separated by wavenumber regions.

within these films. Polarized B-B bonds absorb closer to 1000 cm^{-1}. With an increasing amount of C incorporation the peak shifts toward 1100 cm^{-1} [14]. Thus, the feature at 1105 cm^{-1} is most likely associated with B-C bonding. It has been reported as owing to the B-C stretch in B_4C [31]. The feature at 1240 cm^{-1} may be due to the superposition of contributions from B-C stretching in a C-rich environment and C-C stretching in a B rich environment. The absorbance spectra near 1310 cm^{-1} and 1385 cm^{-1} have been associated with B-O stretch (1350 cm^{-1}) [20] and B-N stretching (1360 cm^{-1} and 1380 cm^{-1}) [32-34]. The shoulder at 1385 cm^{-1} could be due to this B-N stretching mode, considering the XPS data. Although the overall film compositions are poor in N (ranging from 3.3-7.6 at. %), the majority of the constituent N bonding is due to B-N (67-75%). From IR studies of amorphous C:H films that used H-D substitution to remove CH_x bending modes, the C-C skeletal modes were shown to absorb in a broad band between 1300-1400 cm^{-1} and from 1500-1580 cm^{-1} [35]. Combining the IR absorbance assignments with the XPS information, it is reasonable to attribute the higher wavenumber features to both C-C modes made active by the incorporation of B and N in the network as well as B-N stretching modes.

The N-rich BCN films exhibit a main absorbance peak in the region of 850-1600 cm^{-1}. The absorbance peaks for the 300 °C, 360 °C, and 400 °C N-rich films are shown in Fig. 3.8.The shape of these peaks is quite different than those of the C-rich films. Rather than containing many small features over a broad range, these films show absorbance mainly as a shoulder feature around 1110 cm^{-1} and an intense, broad peak centered near 1420 cm^{-1}. As mentioned previously, the absorbance at 1110 has been assigned to the B-C stretching mode. Additionally, the range from 1000-1100 cm^{-1} and more specifically, a peak at 1070 cm^{-1} has been attributed to the B-N stretching mode of the c-BN phase in

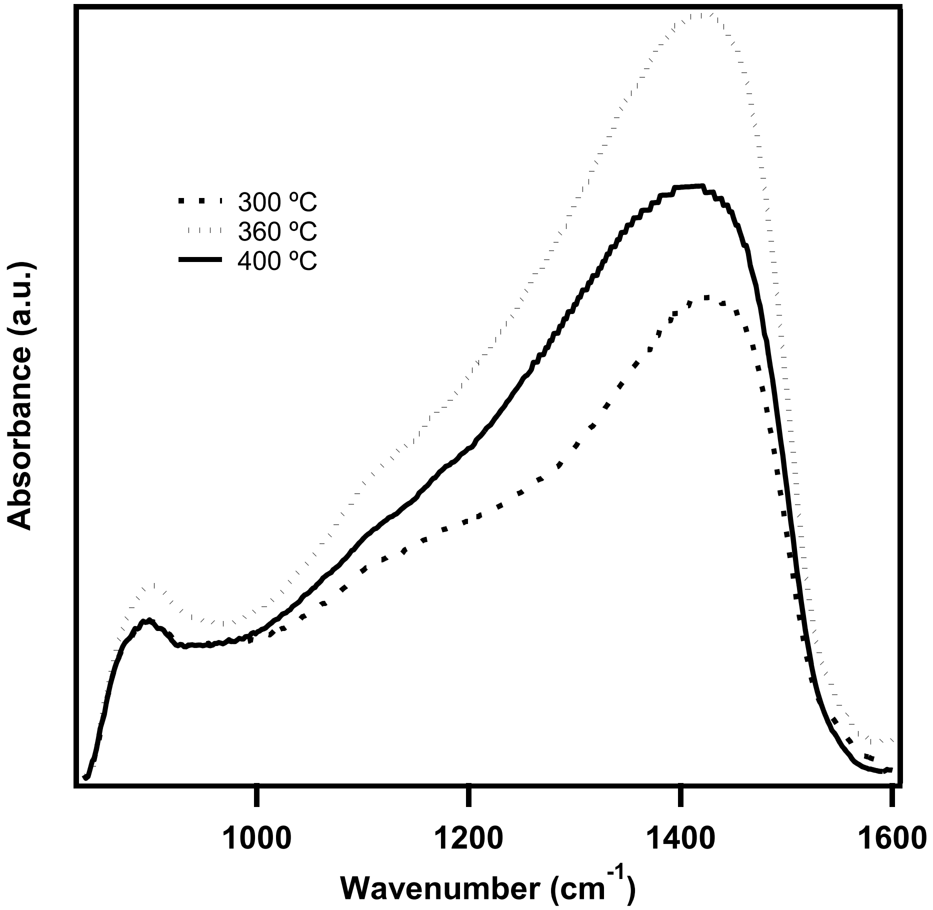

Figure 3.8. FTIR main peak absorbance region for N-rich BCN films deposited from 300-400 °C.

BN films [31,36]. Features at 1420 cm^{-1} and 1450 cm^{-1} have been linked to B-O-N and B-OH modes [33,36]. Since the C content in these films (determined by XPS) is low, the contribution from C-C IR active vibrations is expected to be small. Indeed, there is a characteristic dip in intensity over 1200-1300 cm^{-1} that is indicative of less C-C and B-C modes in the N-rich films. At higher growth temperatures there is an increase in the absorbance in this region. At the same time, the peak centered near 1420 cm^{-1} shifts to a slightly lower wavenumber. This change may be explained by the XPS data. It was shown that as the growth temperature increases for the N-rich films, the constituent B 1*s* bonding shifts to higher B-N contribution and lower B-B contribution. B-C bonding also increases. The additional B-C and B-N bonding causes increased absorbance in the 1100-1200 cm^{-1} region as well as in the 1380 cm^{-1} region. The overall amount of C in the films does not change with growth temperature, but the increasing amount of B-C bonding could introduce more IR active C-C modes. The additional N incorporated in the films at higher temperature along with the increasing B-N bonding contribution is likely responsible for the shift of the peak maximum to lower wavenumber. For all films, there is significant absorbance from 1440-1500 cm^{-1}, which is likely due to the incorporation of oxygen upon exposure to ambient, causing the addition of B-O-N and B-OH vibrational modes.

Figure 3.9 shows the B-H stretching region of both the C-rich and N-rich films. The C-rich films (Fig. 3.9(a)) exhibit a maximum around 2550 cm^{-1} while the N-rich film peak maximum (Fig. 3.9(b)) is closer to 2520 cm^{-1}. A study on amorphous hydrogenated boron films noted that the B-H stretch was observed at 2560 cm^{-1} but upon exposure to atmosphere, the peak intensity increased and shifted to a lower frequency of 2510 cm^{-1}. This is attributed to hydroxylation of the boron films, increasing the effective mass of the

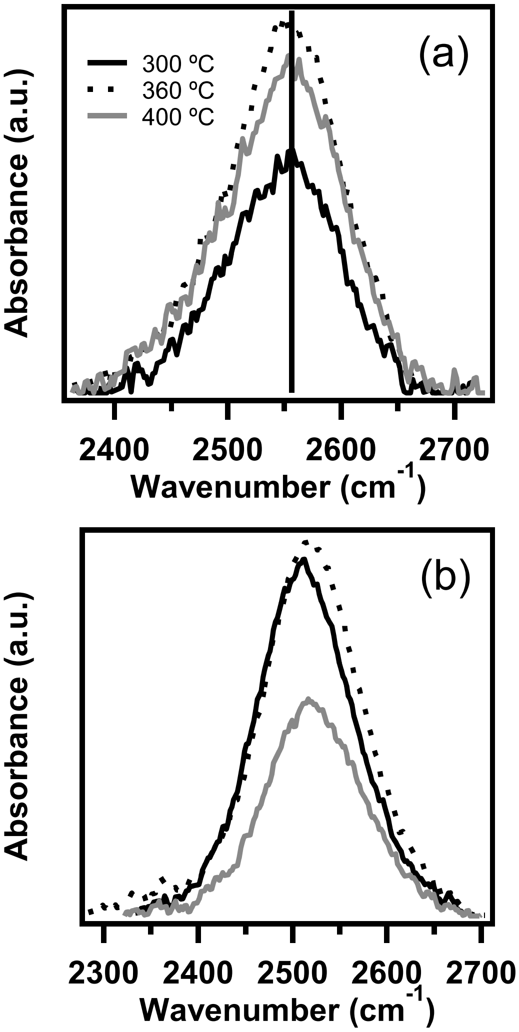

Figure 3.9. FTIR B-H stretch region of (a) C-rich and (b) N-rich BCN films deposited from 300-400 °C. The solid line in (a) denotes a peak maximum near 2550 cm^{-1}.

vibrational mode [17]. It appears that with increasing growth temperature, the N-rich film B-H absorbance peak is shifted further toward higher frequency. The C-rich film B-H absorbance peaks were able to be fit with two Gaussian peaks, indicating that these films were at least partially hydroxylated, yet retained much of the B-H character.

Figures 3.10 and 3.11 show the C-H and N-H stretching features of the C-rich and N-rich BCN films deposited at different temperatures. Deconvolution of the –H stretching region for the N-rich films is also shown. The data was fit with Gaussian peaks using second derivative information. Peak positions were assigned by referenced literature frequencies and allowed to float during the fitting procedure. The shape of the C-H band remains essentially unchanged between the 300 °C and 400 °C N-rich films. In the case of the 360 °C sample, the overall absorbance intensity was enhanced for the entire spectrum. Here, more fine structure of the C-H stretching region is observed, as there are two well defined peaks at 2925 and 2960 cm^{-1}, attributed to the asymmetric modes of sp^3 CH_2 and CH_3 groups, respectively [37]. The peaks below 2850 cm^{-1} are assigned to N-CH_3 and O-CH_3 vibrations [37]. If all modes from the range of 2850-2970 cm^{-1} are lumped together as the contribution from alkyl C-H stretching vibrations and the peak centered at 3050 cm^{-1} is attributed to sp^2 C-H modes, it can be said that there is an overall change in the bonding of these films with increasing growth temperature, from predominantly sp^2 C-H to mainly sp^3 bonded C-H. In the C-H stretching region from 2800-3000 cm^{-1} for the C-rich films, it appears that the peak shape may be shifting with increased growth temperature, but fitting of this portion with the background removed (not shown) reveals surprisingly little change in the individual peak contributions to the signal.

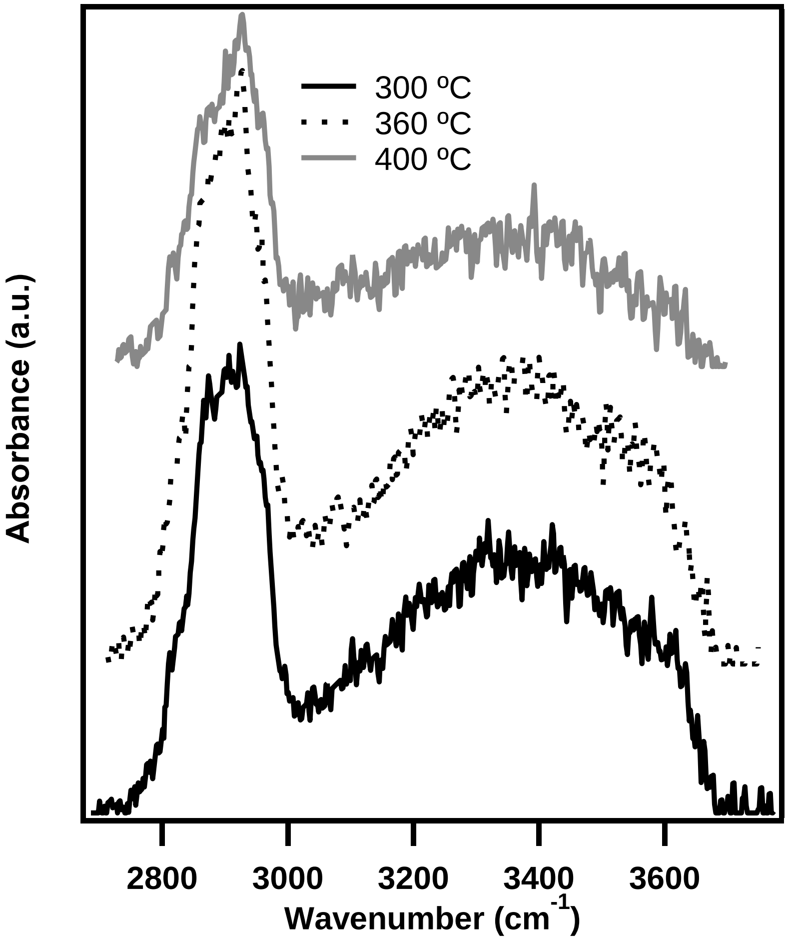

Figure 3.10. FTIR C-H, N-H, and -OH stretching modes of C-rich BCN films deposited from 300-400 °C.

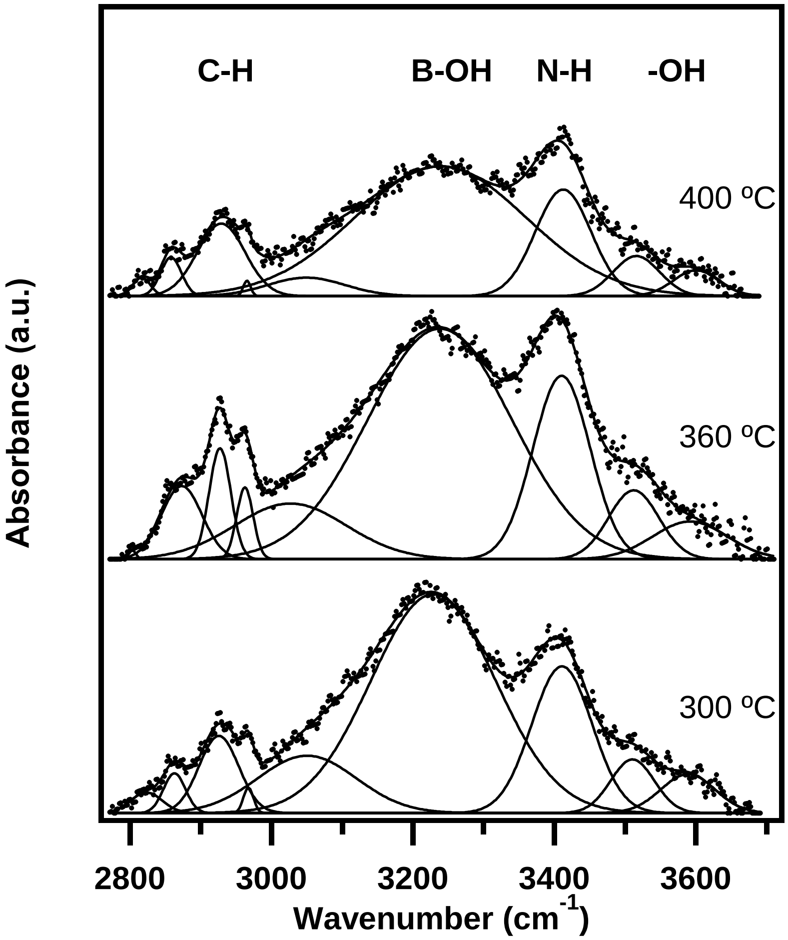

Figure 3.11. FTIR C-H, N-H, and –OH stretching modes of N-rich BCN films deposited from 300-400 °C. Fitted and deconvoluted data are also plotted as thin solid lines. Peak assignments are labeled above the spectra.

The wavenumber range from 3000-3700 cm^{-1} is markedly different between the N-rich and C-rich films. For the N-rich films, there is a clearly defined peak centered at 3400 cm^{-1} that is attributed to N-H stretching modes. Peak deconvolution of this region reveals a fairly broad feature in the range of 3300-3500 cm^{-1}. The aliphatic primary amines absorb at 3375 cm^{-1} and 3310 cm^{-1} for the asymmetric and symmetric stretching modes. The aliphatic secondary amines absorb asymmetrically at 3300 cm^{-1}. The various aromatic and heterocyclic amines absorb at higher wavenumbers (mainly in the range of 3450-3500 cm^{-1}) than the aliphatic molecules, due to an increase in polar character of the NH bond [19]. It appears that the 3400 cm^{-1} peak may be predominantly due to primary aliphatic amines, though it is broad enough to include some of the absorbance region commonly attributed to ring structured amines. Further classification of these modes is not possible due to the broad nature of the peak. In addition, there are two features centered at 3500 cm^{-1} and 3600 cm^{-1}, which may be due to –OH stretching vibrations. These modes have been observed in the literature from 3500-3700 cm^{-1} and are characterized by their broad peaks [19]. Finally, there is a very broad feature centered near 3225 cm^{-1}. This peak may be due to hydroxyl groups attached to B in the film after exposure to ambient. Godet, *et al.*, reported FTIR absorbance features at both 3250 and 3550 cm^{-1} in hydrogenated amorphous boron films and applied this reasoning to explain the peaks [17]. Unlike the N-rich films, the C-rich films do not exhibit the strong feature at 3400 cm^{-1}. This is likely due to the comparatively low N content of these films. Instead, there is a broad, featureless hump over the entire region of interest that is likely a mixture of –OH vibrational modes and N-H stretching modes.

3.3.2. Hydrogen Content

3.3.2.1. SIMS

Figure 3.12 is a representative SIMS profile for a C-rich (3.12(a)) and N-rich (3.12(b)) BCN films. The qualitative difference in the profiles lies in the counts of C and B. In the C-rich film, the counts are higher by almost an order of magnitude. In the N-rich film the B counts are roughly double that of the corresponding C-rich film. All profiles featured relatively flat signals for the secondary ions detected throughout the bulk of the film. The rapid increase of the Si counts signals the film/substrate interface.

The counts for each detected secondary ion species were averaged over the bulk of the film, excluding the nonequilibrium sputtering of the first ~60s of each SIMS profile as well as near the substrate interface. Each average count value was normalized by the average counts of Si from well into the substrate. This ensured that the signal would be corrected for changes in primary intensity or transmission from run to run. These normalized average values are plotted as a function of growth temperature in Fig. 3.13 for C-rich (3.13(a)) and N-rich (3.13(b)) samples. These results suggest that there is a relative increase of H in the N-rich films as growth temperature increases. For the C-rich films, the trend is not linear, and a minimum occurs at 350 °C.

3.3.2.2. FTIR

The relative amount of H incorporated into each film as a function of growth temperature was determined by first normalizing the various –H stretching features in each film by the main absorbance feature from 900-1600 cm^{-1}. Normalization of attenuated total reflectance FTIR data by film thickness is not trivial. Because the technique employs multiple reflections across the sample, the effective thickness is

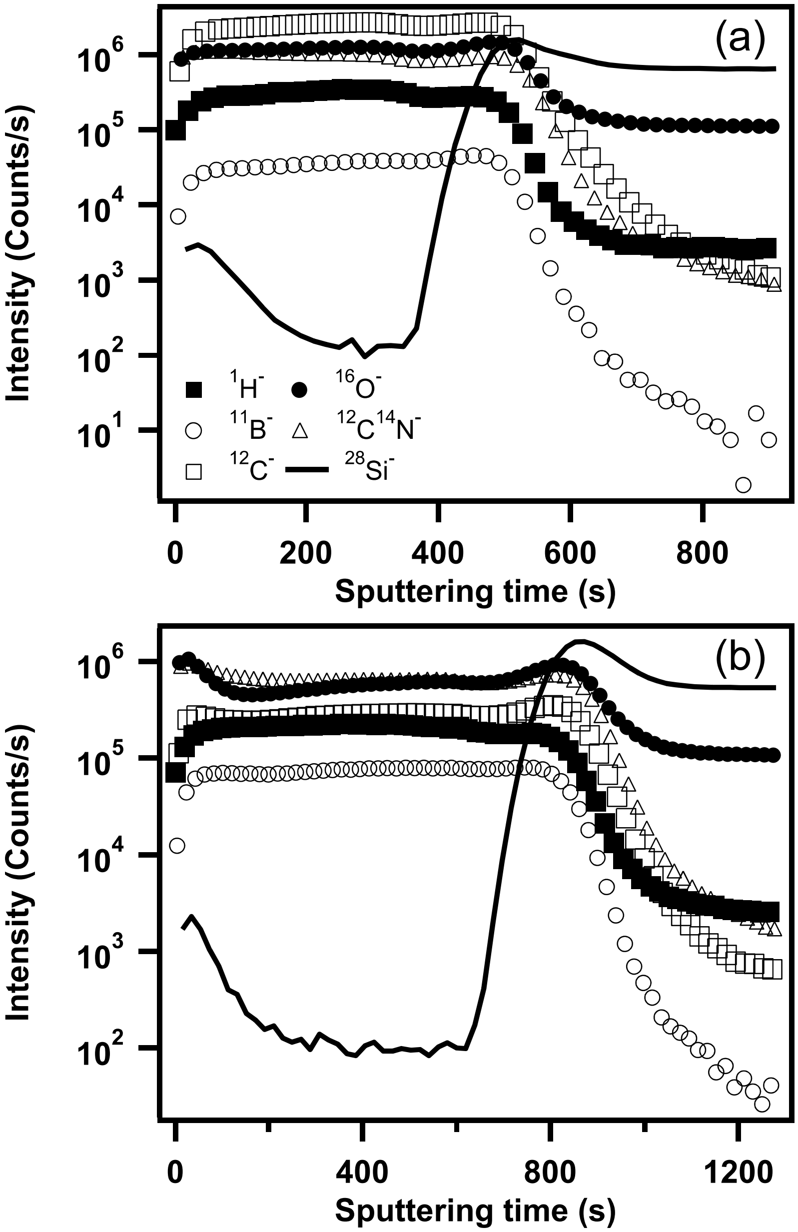

Figure 3.12. SIMS secondary ion depth profiles for (a) C-rich and (b) N-rich BCN films deposited on Si(100). Markers indicate ions from film species. The solid line is the substrate signal.

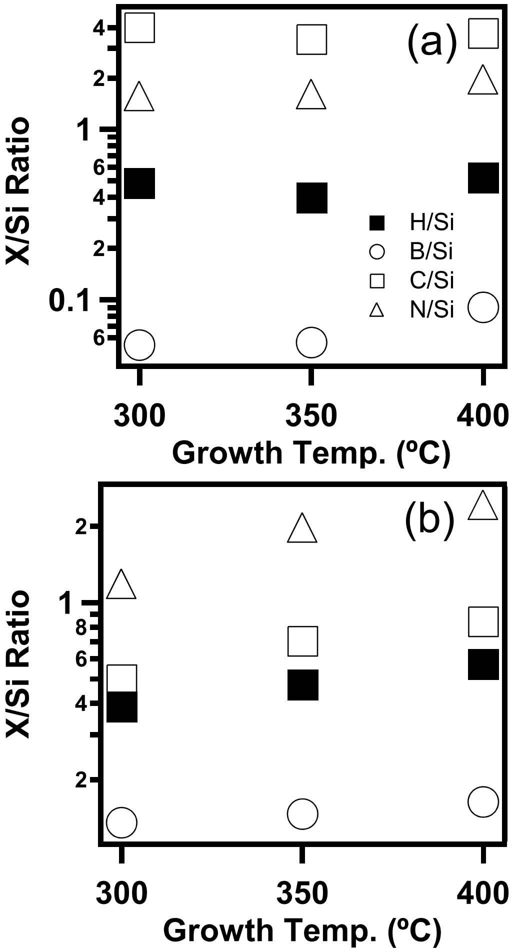

Figure 3.13. Plots of average bulk film ion counts normalized by average bulk substrate counts as a function of growth temperature for (a) C-rich and (b) N-rich BCN films.

dependent on the wavelength of the IR absorbance, the angle of incidence, and the number of internal reflections [38]. However, each set of spectra has a characteristic large absorbance peak representative of the various B, C, and N bonding within the film. Since there is essentially no other constituent bonding other than between these elements and with H, the ratio of areas of the particular H stretching mode to that of the large absorbance peak serves to normalize the data. For both the H stretching features and the main peak features, the peak areas were calculated using PeakFit^{TM} with a suitable number of Gaussian peaks to obtain a reasonable fit. The resulting trend of this normalized data with respect to growth temperature is displayed in Fig. 3.14. It is clear that the N-rich films (3.14(b)) contain relatively more H than the equivalent C-rich film(3.14(a)) at low growth temperatures. At the highest growth temperatures, the H content is almost equivalent. For both the N-rich and C-rich films, the overall H content of the films decreases with increasing growth temperature. In the case of the C-rich films, both N-H and C-H modes decrease with increasing growth temperature, while B-H increases slightly. For the N-rich films, both N-H and B-H bonding decreases, and the contribution from C-H is nearly negligible in comparison.

3.3.3. Valence Band Offset

The valence band offset of different BCN films on Si(100) was measured by the use of Kraut's method [39]. In this method, the valence band maximum of each material is referenced to a shallow core level unique to the material by measuring the energy difference between the two (E_{cl}-E_v) by XPS. Then core level measurements are taken from a sample of the heterojunction. Here, it is important that the overlayer thickness be

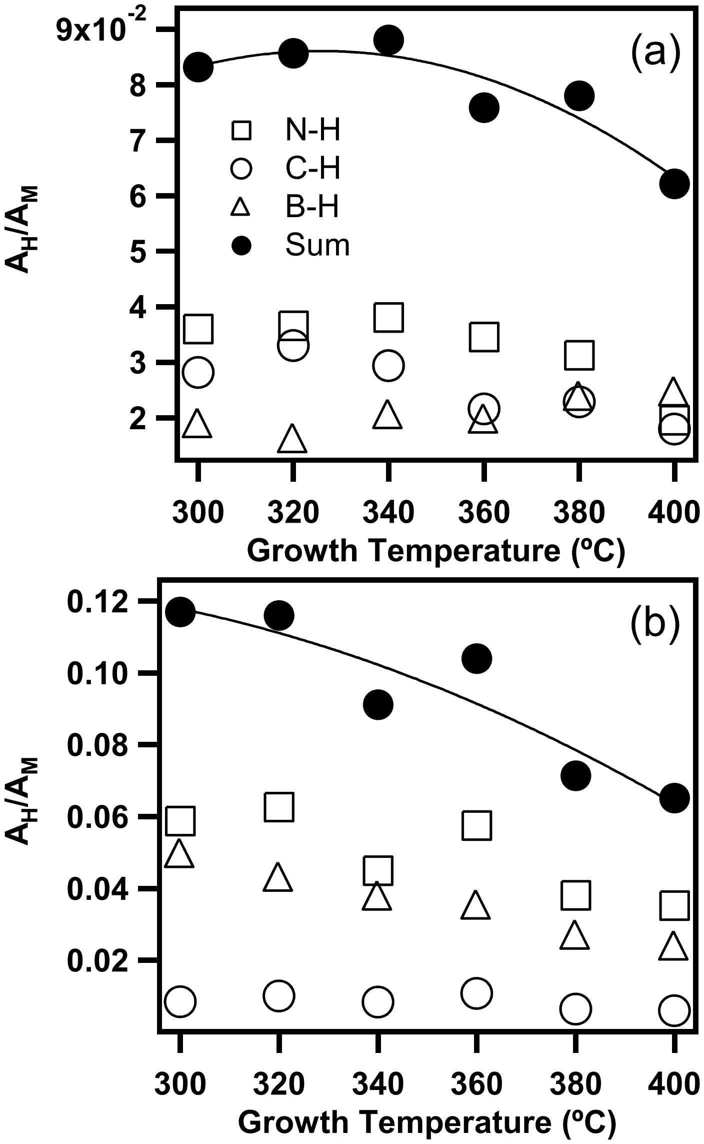

Figure 3.14. Ratio of –H stretching FTIR absorbance areas normalized by FTIR main peak absorbance areas as a function of growth temperature for (a) C-rich and (b) N-rich BCN. The sum of all –H stretching contributions is indicated by the solid markers. The polynomial fit to the data is presented as a guide to viewing the results.

sufficiently small so that XPS contributions from both the deposited film and the substrate are detected. The valence band offset of two materials A and B, is given by

$$\Delta E_v = (E_{cl}^A - E_{cl}^B)_{A/B} - [(E_{cl} - E_v)_A - (E_{cl} - E_v)_B] \tag{3.1}$$

The most difficult value to obtain in this equation is the valence band maximum, E_v. The three most common methods for determining this value involve: (1) fitting a Gaussian valence theoretical density of states to the XPS valence band spectrum; (2) finding the intersection of a least squares fit of the leading edge of the valence band edge with the background; and (3) using UV photoemission to find the energy where the signal at the leading edge falls to zero. Chambers, *et al.*, found that method 1 provided insufficient accuracy while methods 2 and 3 gave physically reasonable results [40].

To calculate the valence band offset for the BCN/Si(100) system, three separate samples were necessary. To obtain $(E_{cl}\text{-}E_v)_B$ a bare Si substrate was analyzed in XPS. Because the signal to noise ratio is low near the valence band edge, the XPS scans in this region were repeated 100 times and the values averaged over the scans. The Si *2p* core level was chosen for analysis of the Si(100) sample. The XPS Signal from the Si 2*p* region is plotted in Fig. 3.15. The valence band maximum region of the Si(100) sample and the linear regression fit used to determine E_v are shown in the inset. The core level binding energy, E_{cl}, was determined by taking the midpoint of the ΔE at the full width at half maximum for the Si 2*p* peak.

Figure 3.16 shows the XPS B 1*s* data for each of the thick BCN films. These data were smoothed and baseline subtracted using a cubic function. The inset of each set of data shows the corresponding valence band maximum determination, found by the

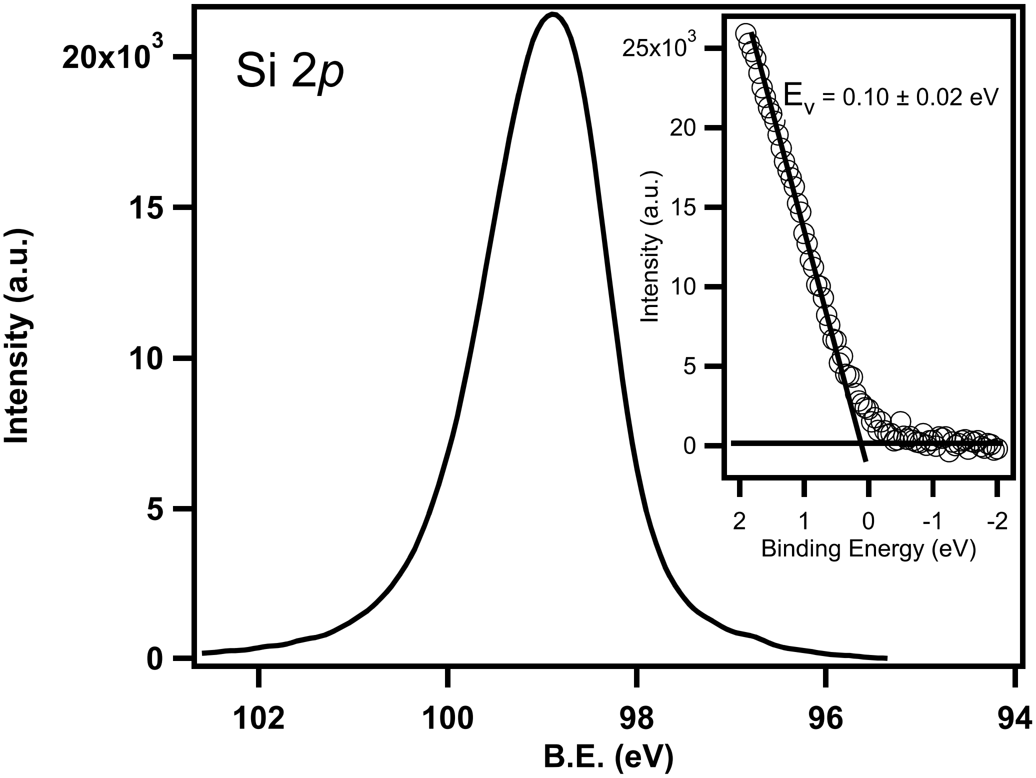

Figure 3.15. XPS Si 2*p* peak of bare Si(100) substrate. The inset is the valence band edge XPS. The valence band maximum (E_v) is determined from the least squares fit of the linear portion of the leading edge and its intersection with the baseline (shown as solid lines).

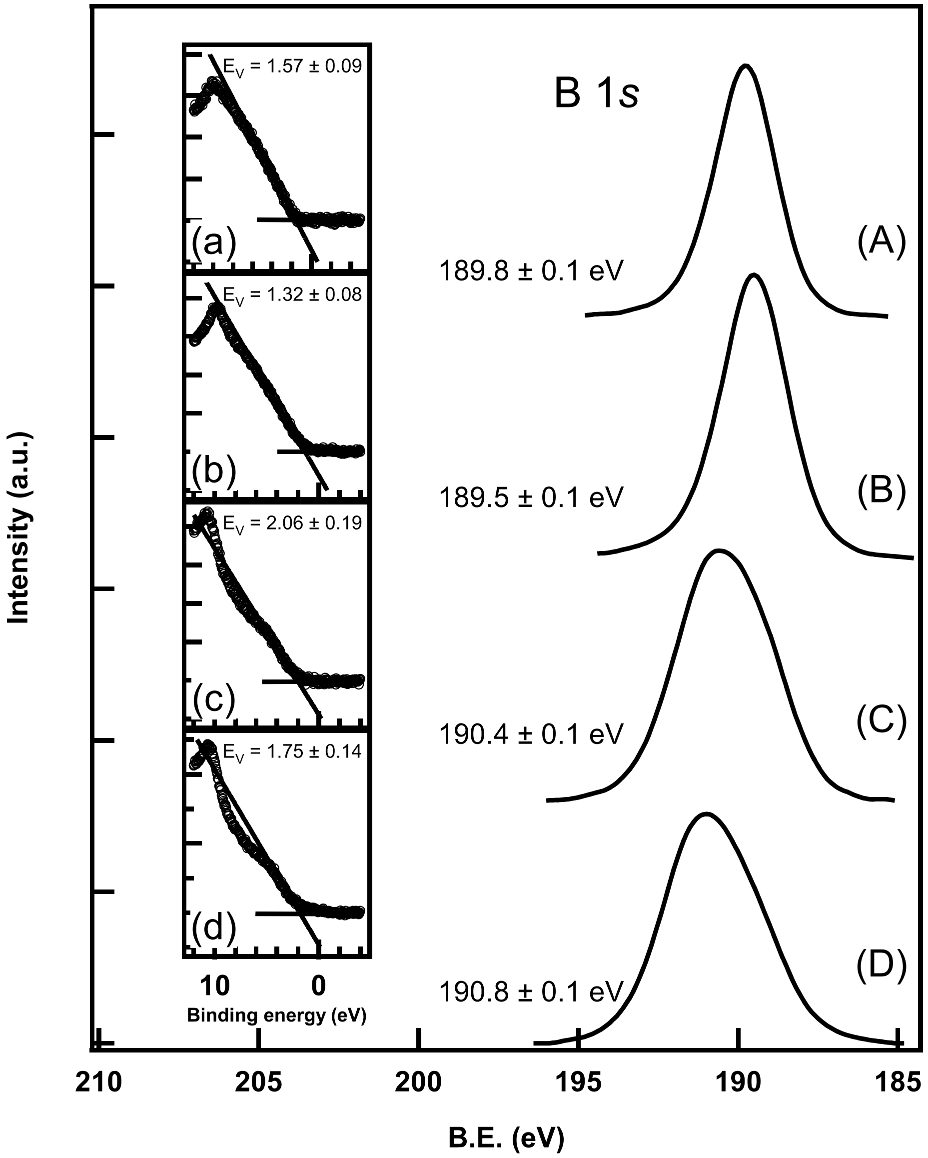

Figure 3.16. B 1*s* XPS of thick (A) 300 °C, (B) 400 °C C-rich and (C) 300 °C, (D) 400 °C N-rich BCN deposited on Si(100). The position of each peak is shown to the left and is determined by the midpoint value of the full width at half maximum. The accompanying valence band spectra are included as insets with corresponding lower case lettering. The valence band maxima (E_v) are determined from the least squares fit of the linear portion of the leading edge and its intersection with the baseline (shown as solid lines).

intersection of the leading edge of the valence band and the background. From these data, the value $(E_{cl} - E_v)_A$ is calculated for each BCN film.

The final value needed to calculate the valence band offset is $(E_{cl}^A - E_{cl}^B)_{A/B}$, which is determined by XPS analysis of a thin BCN film on the Si substrate such that contributions from the core levels of each material are visible in the spectrum. A thin BCN sample was fabricated for each deposition condition, matching the thick BCN films. The core levels used are the B 1*s* of BCN and the Si 2*p* of Si. These data are shown in Fig. 3.17. Each of the peaks were background subtracted, the B 1*s* with a cubic function and the Si 2*p* with a linear function. The data were smoothed and the core level binding energies were determined as the midpoint of the FWHM.

Originally the VBO experiments were undertaken to determine if different interlayers existed between the BCN and the Si substrates when deposited under different conditions. Perego, *et al.*, studied the energy band alignment of the TiO_2/Si system with various interlayers using this method [41]. The problem with direct comparison of this approach with the samples analyzed here is that in the case of the former, the TiO_2 layer is identical for each sample. In the case of BCN, the overlayer is changing in composition and bonding as the deposition conditions are altered. This prevents differentiating between bulk and interfacial effects on the changing band offset. Indeed, the effect of the changing composition of the BCN films on the calculation is seen in the different peak shapes and binding energies of the B 1*s* XPS spectra in Fig. 3.16. There is not a consensus in the literature on whether or not changes in interfacial bonding affects dielectric/semiconductor interfaces. A study comparing abrupt and interlayer containing interfaces for high κ oxides on Si revealed that the band alignment was independent of the interlayer [42].

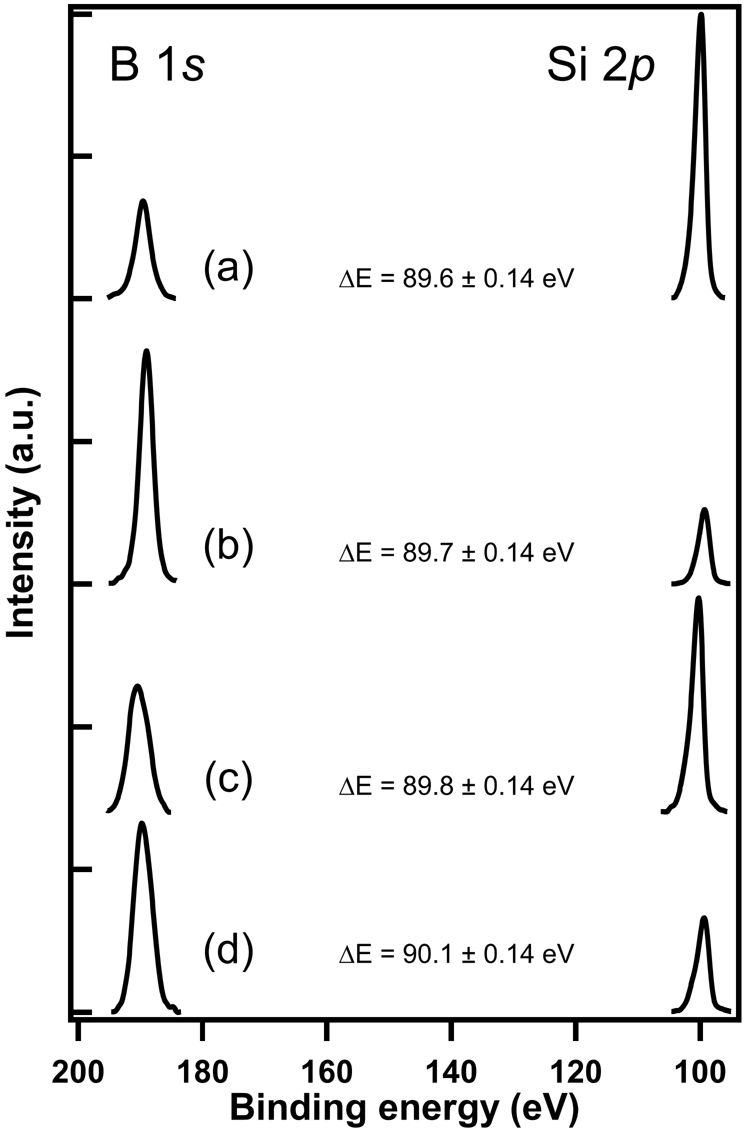

Figure 3.17. B 1*s* and Si 2*p* XPS of thin C-rich (a) 300 °C (b) 400 °C and N-rich (c) 300 °C (d) 400 °C BCN/Si(100). The binding energy difference between the two peaks is shown for each set of XP spectra.

The VBO measurements of the various BCN films suggest that the band offsets change with BCN composition and bonding, as seen in Table 3.1. The optical band gap measurements were determined in a separate study [3]. The conduction band offset values, ΔE_c, are determined using the relation,

$$\Delta E_c = (E_g)_{BCN} - (E_g)_{Si} - \Delta E_v \tag{3.2}$$

where $(E_g)_{BCN}$ and $(E_g)_{Si}$ are the band gaps of BCN and Si, respectively. Note that the errors involved in the measurement of ΔE_v are rather large, on the order of the measurement itself. Unfortunately, increased accuracy is not possible with the current experimental method. The uncertainty associated with each XPS measurement is on the order of 0.1 eV and the propagation of this error across all the measurements required for the VBO result in an accuracy no better than ± 0.2 eV. Additional error is introduced in the least squares fitting of the valence band edge. Regardless, there is enough separation between the measured values to conclude that the offset measurements differ with changing deposition conditions.

3.3.4. Forming Gas Annealing

The XPS deconvolution data for both C-rich and N-rich films before and after forming gas anneals are presented in Table 3.2. The bonding assignments were based on the XPS binding energies of the fitted data along with reported literature references. The left most column labels the main XPS peak on which the deconvolutions were done. The column to the right is the deconvoluted bonding type. As discussed for the above XPS data, the binding energy ranges here suggest a mixed B-B/B-C contribution in the B 1*s*

Table 3.1. Summary of valence band offset measurements ($\mathit{\Delta E_v}$) obtained from XPS analysis of N-rich and C-rich films deposited at substrate temperatures (T_s) of 300 °C and 400 °C. The conduction band offsets ($\mathit{\Delta E_c}$) were calculated from the available optical bandgap information for BCN and the bandgap of Si(100). The optical bandgaps of the C-rich samples are unknown.

BCN Sample	Coreactant gas	T_S (°c)	ΔE_V (eV)	E_g (eV)	ΔC_B (eV)
1	C_2H_4	300	0.17 ± 0.22	-	-
2	C_2H_4	400	0.32 ± 0.22	-	-
3	NH_3	300	0.26 ± 0.28	3.56[a]	2.2
4	NH_3	400	-0.15 ± 0.24	3.25[a]	2.3

[a] Value of optical band gap for sample deposited under identical conditions from Ref. 3

Table 3.2. Comparison of contribution of deconvoluted binding states to the total area of the B 1*s*, C 1*s*, and N 1*s* XP spectra for C-rich and N-rich films deposited at 300-400 °C on Si(100) pre-anneal (left-hand columns) and post 800 °C forming gas anneal (right-hand columns). Spectra were collected after successive sputtering with Ar$^+$ ions to a stable C 1*s* peak to remove contribution from the O contaminated layer.

Deconvoluted Peak Contribution (percentage)							
C-rich BCN							
		300 °C		350 °C		400 °C	
B 1*s*	B-B/B-C	69%	63%	62%	65%	56%	59%
	B-N	25%	29%	31%	28%	38%	33%
	B-O	6%	8%	7%	7%	6%	8%
C 1*s*	C-B	58%	59%	58%	60%	64%	65%
	C-C	37%	36%	36%	33%	31%	30%
	C-C/C-N	5%	5%	6%	7%	5%	5%
N 1*s*	N-B	87%	78%	80%	81%	81%	81%
	N-C	13%	22%	20%	19%	19%	19%
N-rich BCN							
		300 °C		350 °C		400 °C	
B 1*s*	B-B/B-C	33/35%	31/41%	24/37%	20/41%	26/37%	27/39%
	B-N	26%	24%	33%	33%	32%	29%
	B-O	6%	4%	6%	6%	5%	5%
C 1*s*	C-B	54%	70%	72%	69%	60%	74%
	C-C	39%	24%	24%	23%	30%	24%
	C-C/C-N	7%	6%	4%	8%	10%	2%
N 1*s*	N-B	78%	79%	78%	78%	80%	79%
	N-C	22%	21%	22%	22%	20%	21%

deconvolution spectra as well as an overlapping C-C/C-N band in the C 1*s* deconvolution spectra. For the N-rich films the B 1*s* spectra were broader than the C-rich films, suggesting the presence of an additional peak. These spectra were deconvoluted with four peaks. Here, the contribution to either B-B or B-C is quantifiable as separate peaks, and the contribution from each is separated by a forward slash in each column. The temperatures listed are the substrate temperatures for each film growth. There are two columns below each deposition temperature. Each left handed column is the relative amount of the bonding type from the main XPS peak before any annealing. The right handed column contains the relative bonding contributions after the 800 °C anneal. The deconvolution data from the 400 °C and 600 °C anneals are not shown because the overall peak shape changes and BE shifts are small over the entire range of annealing temperature. The addition of the intermediate temperature data does not add to the analysis.

Overall, there is relatively little change in the constituent bonding with forming gas anneal. Generally, there is a shift from B-N to B-C/B-B type bonding and from C-C to C-B type bonding. This is reflected not only in the deconvolution data but the slight shift to lower B.E. for the B 1*s* and C 1*s* peaks (not shown) for XPS data post anneal.

The index of refraction and thickness of the films were determined by spectroscopic ellipsometry as the films were annealed at different temperatures. These results are shown in Fig. 3.18. Here, the open markers indicate the ratio of index of refraction measured before and after annealing, *n*(annealed)/*n*(as-deposited. The closed markers represent the % thickness loss (all films decreased in thickness with annealing). The C-rich (3.18(a)) and N-rich (3.18(b)) films follow the same trend with annealing temperature. As the annealing temperature increases, the index of refraction of all films

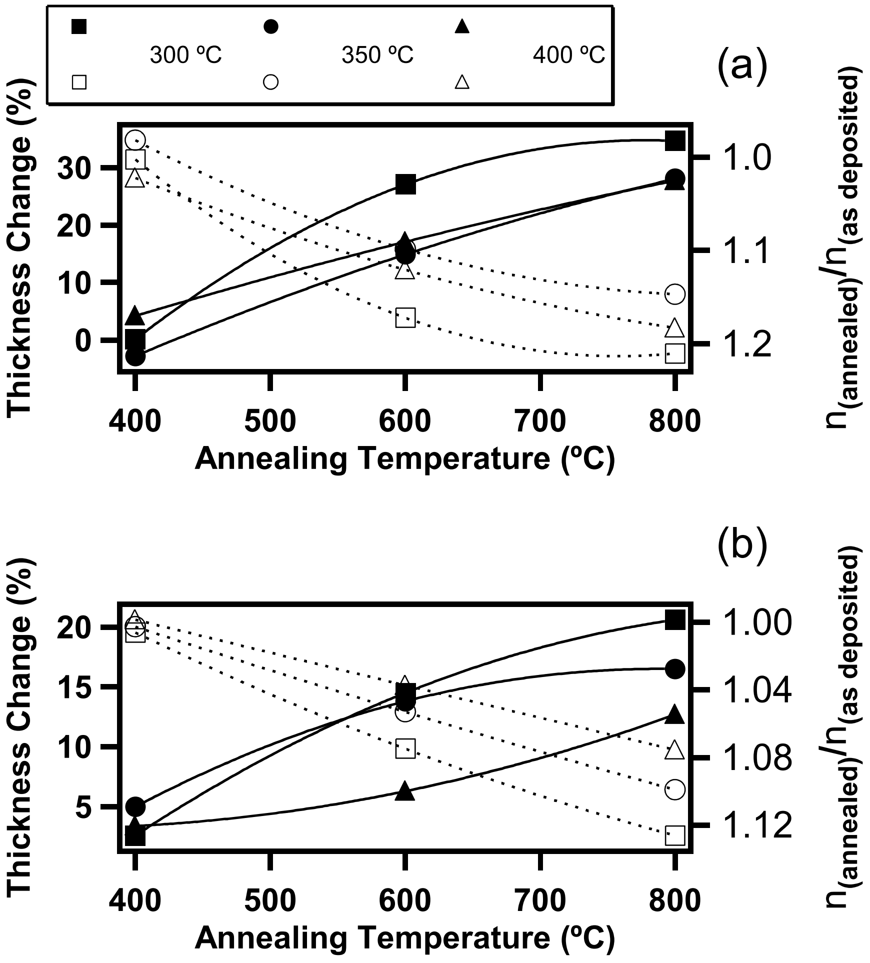

Figure 3.18. Ellipsometric thickness change and ratio of as deposited index of refraction to index of refraction post anneal as a function of forming gas anneal temperature for (a) C-rich and (b) N-rich BCN films deposited on Si(100) from 300-400 °C. Open markers indicate index of refraction ratios and solid markers indicate thickness change (% loss). The fits of the data are presented as a guide to viewing the results.

increases relative to the as-deposited value. Similarly, the film thicknesses decrease as annealing temperature is raised, suggesting that a densification is occurring during the process.

Because there is relatively little change in constituent bonding as detected by XPS, yet the film ellipsometric parameters change drastically for each film as the annealing temperature increases, it may be assumed that volatile –H containing ligands are being removed during the annealing process. Removal of these bulky –H terminated groups would allow for a film with less void fraction, which would explain the decreased thickness and increased index of refraction.

3.4. DISCUSSION

Separate BC and BN zones may be forming in the N-rich films at increasing temperature, as seen in the bonding changes from XPS deconvolution data. B-N-C network bonds decrease at higher temperature. This could be one cause of deteriorating electrical performance. FTIR measurements confirm that these types of bonds are present, with increased absorbance in the 1100 cm^{-1} and 1380 cm^{-1} frequencies. It is not clear what the relative contribution is from c-BN (sp^3 like B-N vibrations) and h-BN (sp^2 like B-N vibrations) from the FTIR data alone. XRD of these BCN films were amorphous [11] and the FTIR peaks are broad, suggesting short range order in an amorphous network. More energy is required for the formation of c-BN and as a result, there could potentially be more sp^3-like B-N bonding in the N-rich films deposited at higher temperature. Cubic BN films exhibited donor traps and n-type conduction [43]. The counterclockwise hysteresis observed from N-rich BCN MIS devices also suggested donor traps in the bulk of the film. Clockwise hysteresis was also found on devices without an SiO_2 layer between the BCN and the Si substrate, indicating that acceptor traps also existed in these films [3]. A study of C containing h-BN films found the impurity C substituted for N, resulting in acceptor traps [44]. Boron carbide without doping is a p-type semiconductor. This could also be a source of acceptor traps in the N-rich films, since there is a significant amount of C in every film. The deconvoluted XPS data show a large contribution of B-C bonding in the B 1*s* spectrum, increasing with increasing growth temperature.

The C-rich films display a broad, multicomponent FTIR peak in the region of 1000-1400 cm^{-1}. The absorbance from 1000-1300 cm^{-1} is indicative of B-B and B-C stretching vibrations surrounded by a matrix of varying B and C concentration. The shoulder region from 1300-1400 cm^{-1} represents B-O and B-N stretching vibrations. Following the reasoning used in the structure of the N-rich films, the structure of the C-rich films may be assumed to be BC-like with an impurity level of N, when deposited at low temperature. As more energy is supplied to the system, the composition becomes rich in B and poor in C, and more N is incorporated into the films. Compositionally, the C-rich films approach that of the N-rich films at the high end of the temperature window. However the C content remains elevated. The C that remains becomes increasingly bound to B. The increased N network bonds as B-N-C at the expense of N-B. The B in the film becomes increasingly bound to C, mirroring the deconvoluted C 1*s* spectra. The sum of these changes seems to indicate that N may serve to counteract the naturally p-type conducting BC material.

Positive flatband voltage shift in C-rich MIS devices indicated the existence of fixed negative charge in the films. A possible explanation for this was sp^2 hybridized C bonds [3]. The presence of olefinic C=C and C=N moieties in the C-rich and N-rich films is not supported by the FTIR data. These stretching vibrations were assigned to 1500-

1600 cm^{-1}, and 1540-1550 cm^{-1} for C=C and C=N, respectively [13,31,45]. The C-rich main absorbance peak does not extend to these wavenumbers, ruling out any contribution from these modes. There could be a small shoulder in the N-rich spectra, owing to these absorbances, but the main peak is shifted to lower wavenumbers. While the XPS N 1*s* and C 1*s* spectra contained deconvoluted peaks with binding energies that could be assigned to C=N and C=C bonding, the lack of supporting data from FTIR suggests these peaks originate from different bonding environments. The fixed negative charge could be due to N incorporated into the film as an impurity donor. Perhaps not all N in the film is bound to B or C.

The FTIR spectra revealed that H bonding occurs in both the C-rich and N-rich films. The H bonding absorbance peaks are strongest for the majority compositional species in the film, i.e. B-H and N-H bonding for the N-rich films, and B-H and C-H bonding in the C-rich films. For all films, the raw absorbance data shows no features associated with sp^2 C-H modes, though the contribution from these modes may be masked by overlapping absorbance from the N-H/-OH active modes. Deconvolution of the N-rich film data in this region seemed to suggest the presence of sp^2 C-H modes in a broad peak centered around 3050 cm^{-1} but it is unclear how physically meaningful the deconvolution data is in this region. The absorbance of sp^3 modes is stronger than that of the assigned sp^2 mode, as it does not appear in the raw spectrum. It may be assumed that the majority of H bonded to C is sp^3 hybridized. No meaningful trends emerge from the positions of the various –H stretching modes as a function of temperature.

Quantifying the amount of H incorporated in these films proved to be difficult. The SIMS data of these films showed a relative increase in H content of the N-rich films with increasing growth temperature. However, the relative C, B, and N signals also increased nearly linearly as the temperature increased. This does not follow the XPS compositional data, which shows a trend of decreasing B and nearly constant C content. It is well known that the SIMS technique suffers from the matrix effect, where the secondary ion sputter yield and ionization probability are highly dependent on the bonding environment of the species ejected from the substrate [46]. Detection of MCs^+ (where M denotes a neutral species of interest) clusters was attempted first. Here, neutral atoms that are ejected during the sputtering process are bound to Cs^+ ions after emission. Under this mode of detection, matrix effects are greatly reduced since the analyzed ions do not originate from the surface and the ion yield does not depend on the local concentration of the film. However, the sensitivity of the measurement is greatly reduced. For BCN films, the signal was too weak for accurate measurement. Measurement of the ejected secondary ions in the negative mode (M^-) provided the SIMS data for this study. For true quantitative SIMS, the use of relative sensitivity factors is necessary to convert the ion intensities to concentrations. Calibration samples of known concentration must be analyzed first to obtain the sensitivity factors [47]. This requires a separate analytical technique to quantify the H content of the films, rendering the SIMS analysis unnecessary.

The FTIR -H absorbance areas normalized to the broad main peak absorbance areas provided a method to compare the H content in each film relative to the other vibrational modes. Fitzpatrick proposed that N-rich films behave better electrically because dangling bonds are removed by the reactive NH_3 species during deposition [3]. The FTIR results support this idea by showing that more H is incorporated into the NH_3 coreacted films, the majority in the form of B-H and N-H bonds. The overall H content in these films decreases as a function of temperature, which trends with the deteriorating CV curves of the higher temperature deposited N-rich devices. At low temperature, the relative H content of the C-rich films is half that of the N-rich films, supporting that C-rich BCN may have more dangling bonds that serve as surface states or fixed negative charge. These results may point to higher relative absorbances than would be obtained from samples analyzed in vacuum. Because the N-H and O-H stretching regions share common wavenumbers. It is not clear how much of the N-H assigned absorbance is actually due to water absorbed in the films upon exposure to ambient. Fitzpatrick has documented the oxygen uptake of these films upon exposure to ambient. It is reasonable to expect that some of this oxygen incorporation is due to absorbance of water [30]. Both types of films showed evidence of moisture uptake. Interaction with the ambient was seen in the N-rich films with FTIR contributions from B-O, B-OH, and broad –OH stretching region. The C-rich films showed little evidence from the former two contributions but featured the broad –OH stretching region in the absence of a sharp N-H stretching signal.

Understanding the band structure of the BCN/Si heterojunction provides insight into possible modes of charge transfer in MIS BCN devices. Previous electrical testing of MIS capacitor devices utilizing BCN alone or in series with HfO_2 or SiO_2 as the insulator showed that C-rich BCN films suffered from large flatband voltage shifts and this was attributed to fixed negative charge within the bulk of the films [3]. Counterclockwise hysteresis observed in the C-rich devices suggested the existence of donor traps in the BCN. Under positive bias (accumulation condition for n-type Si) the semiconductor band bending coupled with the large amount of negative charges present in the insulator could allow for significant hole current from the insulator to the semiconductor. The VBO measurements of the C-rich films indicate that the band offset between BCN/Si increases with films deposited at higher growth temperature. If the main pathway for current transfer in these devices is through hole conduction, it would be expected that the C-rich devices with BCN deposited at higher deposition temperature would perform better electrically.

N-rich films were shown to have more flatband voltage shift, hysteresis, and leakage when deposited at higher growth temperature [3]. The VBO measurements for the N-rich films are in agreement with these findings. Since the conduction band offset of these junctions is > 1 eV, and given that the VBO between BCN/Si is < 0.54 eV in the best case scenario, it is likely that the pathway for conduction is from either hole injection at the gate or hole transfer at the BCN/Si interface. The pathway for hole transfer is made easier by a decreased valence band offset in the film grown at higher temperature. Although no concise explanation is given for the physical description of these traps, it is clear that the constituent bonding changes across the process temperature range, resulting in an increase of defects in the BCN with increased growth temperature. In the discussion of the XPS and FTIR data it was suggested that the defects arose from bonding changes in the film and associated charge traps. The H content data provided evidence that increased amounts of dangling bonds could exist in the C-rich films and high temperature deposited N-rich films. The presence of these defects is evident in the electrical testing results as well as the VBO measurement and the optical bandgap.

The BCN film properties changed unfavorably with high temperature anneals in forming gas. Because there is relatively little change in constituent bonding as detected by XPS, yet the film ellipsometric parameters change drastically for each film as the annealing temperature increases, it may be assumed that volatile –H containing ligands are being removed during the annealing process. Removal of these bulky –H terminated groups would allow for a film with less void fraction, which would explain the decreased thickness and increased index of refraction. A study on annealing of diamond-like carbon films found a significant decrease in the absorbance of $C(sp^3)$-H stretching after anneals from 350-650 °C. The optical band gap energy was also found to decrease after annealing [48]. The index of refraction and thickness of SiCOH films decreased with annealing, due to the loss of CH_x groups, as determined by FTIR [8]. Annealing of H containing BN films resulted in B-H loss from 673-923K and N-H loss above 973 K [49]. It is likely that the difference between the SiOCH and BCN index of refraction changes with annealing is due to a strong cage structure that exists in the SiOCH film. Removal of the volatile species actually increases void volume in this case. The BCN films may be densifying, which would explain the increase in index of refraction. Since the optical dielectric function goes as n^2 (assuming no absorption at the wavelength of the measurement), the dielectric constant of these films is probably increasing due to the annealing process [50].

Adopting the relative H content information from the FTIR studies and applying it to these annealing studies, if the species being removed from the films are mostly –H containing species, the relative thickness change should be sensitive to the amount of H incorporated in the films at different growth temperature. It is seen in Fig. 3.18 that the thickness change decreases as a function of growth temperature, just as the relative H content of the films decreases with increasing growth temperature.

3.5. SUMMARY

BCN films were deposited on Si(100) at different growth temperatures from 300-400 °C and were enriched in C or N by coreaction with C_2H_4 or NH_3 process gases. The atomic compositions and relative bonding as a function of growth temperature were determined through XPS analysis. Additional bonding information, including –H bonding was studied with FTIR measurements. C-rich films became concentrated in B and N at the expense of C at higher temperature, approaching a composition closer to that of the N-rich films. The constituent bonding shifted from C-C and B-B to intermixed C-B/B-C bonds. The N-rich films were reduced in B concentration and enriched in N, while C stayed constant with increasing temperature. Constituent bonding shifted to B-C, B-N, and N-B. C-N and N-C bonding was a small contribution to the C 1*s* and B 1*s* spectra of all films. FTIR of the BCN films supported these findings, and proved that H bonding exists for the films at all reaction conditions. The relative amounts of hydrogen decreased with increasing temperature for both C-rich and N-rich films, and N-rich films had roughly twice the H absorbance as C-rich films at 300 °C. Olefinic bonds were not detected with FTIR. SIMS was also used to probe the H content of the films, but the results were not in line with XPS findings.

The valence band offsets of N-rich and C-rich films deposited at 300°C and 400°C were determined by XPS analysis. N-rich films had a decreasing VBO at higher temperature, suggesting that the barrier to charge transfer is lowered with films deposited at elevated temperature. The C-rich films displayed the opposite trend.

High temperature anneals from 400-800 °C were performed on BCN/Si samples. The film thickness decreased while the index of refraction increased for all samples with annealing. The amount of thickness reduction scaled with the amount of H incorporated in the films. It is likely that volatile CH_x, BH_x, and NH_x groups are removed from the films during annealing. XPS revealed no major changes in constituent bonding other than a slight shift from B-N to B-C and C-C to C-B. The increasing index of refraction is the result of film densification. Although the dielectric constant was not measured from MIS devices, it can be expected to increase as the square of the index of refraction.

3.6. REFERENCES

[1] Engbrecht, E.R., Sun, Y.-M., Junker, K.H., White J.M., Ekerdt, J.G., *J. Vac. Sci. Technol. B*, 23, pp. 463-467; 2005.

[2] Ahearn, W.J., Fitzpatrick, P.R., Ekerdt, J.G., *J. Vac. Sci. Technol. A*, 25, pp. 570-574; 2007.

[3] Fitzpatrick, P.R., Ekerdt, J.G., *J. Vac. Sci. Technol. B*, 27, pp. 2366-2374; 2009.

[4] Speranza, G., Minati, L., *Diamond and Related Materials*, 16, pp. 1321-1324; 2007.

[5] Engbrecht, E.R. Sun, Y.-M., Junker, K.H., White, J.M., Ekerdt, J.G., *J. Vac. Sci. Technol. A*, 22, pp. 2152-2158; 2004.

[6] Umeda, S., Yuki, T., Sugiyama, T., Sugino, T., *Diamond and Related Materials*, 13, pp. 1135-1138; 2004.

[7] Sugiyama, T., Tai, T., Sugino, T., *Applied Physics Letters*, 80, pp. 4214-4216; 2002.

[8] Lee, S., Yang, J., Yeo, S., Lee, J., Jung, D., Boo, J.-H., Kim, H., Chae, H., *Japanese Journal of Applied Physics*, 46, pp. 536-541; 2007.

[9] Grill, A, Patel, V., *Applied Physics Letters*, 79, pp. 803-805; 2001.

[10] Milella, A., Delattre, J.L., Palumbro, F., Fracassi, F., d'Agostino, R., *Journal of the Electrochemical Society*, 153, pp. F106-F114; 2006.

[11] Engbrecht, E.R., Dissertation, The University of Texas at Austin; 2004.

[12] Moulder, J.F., Stickle, W.F., Sobol, P.E., Bomben,K.D., Handbook of X-ray Photoelectron Spectroscopy. Eden Prairie, MN: Physical Electronics, Inc.; 1995.

[13] Essafti, A., Ech-chamikh, E., Fierro, J.L.G., *Diamond and Related Materials*, 14, pp. 1663-1668; 2005.

[14] Linss, V., Rodil, S.E., Reinke, P., Garnier, M.G., Oelhafen, P., Kreissig, U., Richter, F., *Thin Solid Films*, 467, pp. 76-87; 2004.

[15] Yue, J., Cheng, W., Zhang, X., He, D., Chen, G., *Thin Solid Films*, 375, pp. 247-250; 2000.

[16] Abdul Mannan, M., Nagano, M., Kida, T., Hirao, N., Baba, Y., *Journal of Physics and Chemistry of Solids*, 70, pp. 20-25; 2009

[17] Godet, C., Schmirgeld, L., Zuppiroli, L., Sardin, G., Gujrathi, S., Oxorn, K., *Journal of Material Science*, 26, pp. 6408-6418; 1991.

[18] Bellamy, L.J., The Infrared Spectra of Complex Molecules. London, England: Chapman and Hall; 1975.

[19] Wexler, A.S., *Applied Spectroscopy Reviews*, 1, pp. 29-98; 1967.

[20] Saß, M., Annen, A., Jacob, W., *J. Appl. Phys.*, 82, pp. 1905-1908; 1997.

[21] Billa, R.B., Hofmann, T., Schubert, M., Robertson, B.W., *Journal of Applied Physics*, 106, pp. 033515 1-4; 2009.

[22] Lin, S.-H., Feldman, B.J., *Applied Physics Letters*, 69, pp. 2373-2375; 1996.

[23] Schulz, D.L., Lutfurakhmanov, A., Mayo, B., Sandstrom, J., Bunzow, D., Qadri, S.B., Bao, R., Chrisey, D.B., Caruso, A.N., *J. Non-Crystalline Solids*, 354, pp. 2369-2371; 2008.

[24] Bounouh, Y., Thèye, M.L., *Physical Review B*, 51, pp. 9597-9604; 1995.

[25] von Keudell, A., Jacob, W., *J. Vac. Sci. Technol. A*, 15, pp. 402-407; 1997.

[26] Annen, A., Saß, M., Beckmann, R., von Keudell, A., Jacob, W., *Thin Solid Films*, 312, pp. 147-155; 1998.

[27] Mondal, S., Banthia, A.K., *Journal of the European Ceramic Society*, 25, pp. 287-291; 2005.

[28] Essafti, A., Ech-chamikh, E., Azizan, M., *Spectroscopy Letters*, 41, pp. 57-63; 2008.

[29] Hammer, P., Baker, M.A., Lenardi, C., Gissler, W., *Thin Solid Films*, 290-291, pp. 107-111; 1996.

[30] Fitzpatrick, P.R., Dissertation, The University of Texas at Austin; 2009.

[31] Ling, H., Wu, J.D., Sun, J., Shi, W., Ying, Z.F., Li, F.M., Diamond and Related Materials, 11, pp. 1623-1628; 2002.

[32] Morant, C., Prieto, P, Bareno, J., Sanz, J.M., Elizalde, E., *Thin Solid Films*, 515, pp. 207-211; 2006.

[33] Anutgan, M., Aliyeva Anutgan, T., Ozkol, E., Atilgan, I., Katircioglu, B., *Journal of Non-Crystalline Solids*, 355, pp. 1622-1629; 2009.

[34] Dalui, S., Pai, A.K., *Vacuum*, 82, pp. 1296-1301; 2008.

[35] Ferrari, A., Rodil, S., Robertson, J., *Physical Review B*, 67, pp. 155306 1-20; 2003.

[36] Yasui, H., Awazu, K., Ikenaga, N., Sakudo, N., *Vacuum*, 83, pp. 582-584; 2009.

[37] Titus, E., Misra, D.S., Sikder, A.K., Tyagi, P.K., Singh, M.K., Misra, A., Ali, N., Cabral, G., Neto, V.F., Gracio, J., *Diamond & Related Materials*, 14, pp. 476-481; 2005.

[38] Stein, H.J., Wegener, H.J.R, *J. Electrochem. Soc.*, 124, pp. 908-912; 1977.

[39] Kraut, E.A., Grant, R.W., Waldrop, J.R., Kowalczyk, S.P., *Phys. Rev. Lett.*, 44, pp. 1620-1623; 1980.

[40] Chambers, S.A., Droubay, T., Kaspar, T.C., Gutowski, M., *J. Vac. Sci. Technol. B*, 22, pp. 2205-2215; 2004.

[41] Perego, M., Seguini, G., Scarel, G., Fanciulli, M., Wallrapp, F., *Journal of Applied Phyics*, 103, pp. 043509-1-6; 2008.

[42] Afanas’ev, V.V., Stesmans, A., Edge, L.F., Scholm, D.G., Heeg, T., Schubert, J., *Applied Physics Letters*, 88, pp. 032104 1-3; 2006.

[43] Phani, A.R., Manorama, S., Rao, V.J., *Semicond. Sci. Technol.*, 10, pp. 1520-1522; 1995.

[44] Kawaguchi, M., Nozaki, K., Kita, Y., Doi, M., *Journal of Materials Science*, 26, pp. 3926-3930; 1991.

[45] Podder, J., *Modern Physics Letters B*, 21, pp. 455-466; 2007.

[46] Hofmann, S., Rar, A., Moon, D.W., Yoshihara, K., *J. Vac. Sci. Technol. A*, 19, pp. 1111-1115; 2000.

[47] Dreer, S., Wilhartitz, P., Piplits, K., Mayerhofer, K., Foisner, J., Hutter, H., *Anal. Bioanal. Chem.*, 379, pp. 599-604; 2004.

[48] Akkerman, Z.L., Efstathiadis, H., Smith, F.W., *Journal of Applied Physics*, 80, pp. 3068-3074; 1996.

[49] Akkerman, Z.L., Kosinova, M.L., Fainer, N.I., Rumjantsev, Yu.M., Sysoeva, N.P., *Thin Solid Films*, 260, pp. 150-160; 1995.

[50] Morgen, M., Ryan, E.T., Zhao, J.-H., Hu, C., Cho, T., Ho, P.S., *Annu. Rev. Mater. Sci.*, 30, pp. 645-680; 2000.

Chapter 4: Summary

4.1. CONCLUSIONS

BCN was evaluated as a pore sealing layer on blanket and patterned pMSQ substrates. Films of varying thicknesses were deposited on blanket substrates, exposed to TaF_5 for 60s, and analyzed by XPS depth profiling and backside SIMS. The Ta signal was monitored in XPS to determine the penetration depth of TaF_5 into the sample. Films that exhibited attenuation of the Ta signal to <2% before reaching the calculated BCN/pMSQ interface were considered successful at sealing the porous interface. Backside SIMS confirmed that the residual Ta signal was due to Ar^+ ion knock-in effect from sputtering. Progressively thinner layers of BCN were analyzed and the minimum thickness film that was able to seal the pMSQ was 3.9 nm. Annealing of the 3.9 nm sample at 370 °C for 40 min resulted in no change in the depth profile, suggesting BCN is thermally stable. Patterned pMSQ substrates were utilized to simulate a geometry more representative of that found in a dual damascene process. BCN samples deposited on patterned samples were coated with $TaSi_x$ films and sidewall structures were analyzed by EELS/EDXS to determine the compositional variation across the feature. A 3.9 nm BCN film was sufficiently thick to prevent penetration of Ta into the pMSQ of these patterned substrates. The B signal attenuated into the porous dielectric but a baseline amount persisted throughout the substrate. This indicates that DMAB is diffusing into the low κ. The BCN/pMSQ interface is not abrupt. Nucleation and growth may occur inside pore mouths, which suggests the pore size distribution and connectivity is important in controlling the extent of BCN growth into the porous substrate.

The various types of chemical bonding in BCN films were probed using XPS and FTIR. The material exhibited a large compositional variation with growth temperature from 300-400°C. Films deposited with C_2H_4 coreactant gas had a high C and B %. The C-rich films became concentrated in B at the expense of C as growth temperature increased. The N concentration remained below 10 at. % and increased with higher growth temperature. Films deposited with NH_3 coreactant gas were rich in B and N, and contained little C. The %N increased while B decreased with increasing growth temperature. The deconvoluted XP spectra revealed that intermixing of C and B occurred with higher growth temperature for C-rich films. The N-rich films showed increased B-N bonding with higher temperature. FTIR absorbance peaks were identified for B, C, and N stretching vibrations as well as for –H stretching vibrations. C-rich films exhibited large C-H and B-H stretching vibrations. N-rich films contained C-H, B-H, and N-H stretching frequencies. The relative H content of BCN as determined by FTIR showed a trend of decreasing H content with higher growth temperature for both C-rich and N-rich films. N-rich BCN had roughly twice the H content of C-rich films deposited at 300 °C.

The heterojunctions of BCN/Si(100) structures were investigated by XPS. Using a technique involving the core level binding energies and valence band edges of the pure BCN and Si(100) as well as the core level binding energies of thin BCN/Si(100) substrates the valence band offset was determined for C-rich and N-rich films deposited at 300 °C and 400 °C. The VBO changed from 0.17 ± 0.22 eV to 0.32 ± 0.22 eV for the C-rich films grown at 300 °C and 400°C. N-rich films had the opposite trend with temperature, decreasing from 0.26 ± 0.28 at 300 °C to -0.15 ± 0.24 eV at 400 °C. These results suggest that C-rich BCN may exhibit lower leakage when deposited at higher growth temperature.

High temperature forming gas anneals of C-rich and N-rich BCN films from 400-800 °C caused the film thickness to decrease and the index of refraction to increase for all samples tested. The minor changes in XPS bonding within the films post annealing suggests that volatile CH_x, BH_x, and NH_x groups are removed during the process, resulting in film densification.

4.2. RECOMMENDATIONS FOR FUTURE WORK

Though BCN is able to function as a pore sealing layer, much work remains to determine if it may ultimately serve as an insulating diffusion barrier. The nature of the fixed negative charge in the C-rich films has not been fully explained. FTIR did not reveal the expected C π-bonding. Engbrecht suggested that B-N bonding may be an additional source of delocalized bonding, and the FTIR vibrational frequencies suggest the presence of both sp^2 and sp^3 like B-N modes. Confirmation of these results should be sought in ultraviolet photoelectron spectroscopy, where the valence band may be studied for changing π character. Raman spectroscopy, with enhanced sensitivity to distributed electron clouds, could provide additional information about the carbon bonding that is not detected in FTIR.

In chapter 3, FTIR results indicated that both C-rich and N-rich BCN films may absorb moisture from the ambient. This is an undesirable process, as water could drastically change the dielectric constant of the insulator and impede adhesion. Dielectric constant testing of MIS capacitors in ambient and in an inert environment post anneal could aid in understanding the extent of this moisture absorption issue.

The ultimate hindrance for BCN as a diffusion barrier may be its electrical performance. As an insulator it has yet to be successfully integrated into a MIS test structure without a supporting oxide such as SiO_2 or HfO_2. The performance of BCN as the sole insulating material is an important experimental result because these films are envisioned for use as a diffusion barrier or as a capping layer. High leakage and evidence of bulk and interfacial traps in both C-rich and N-rich BCN films present significant integration challenges. While C-rich BCN films were found to be the best Cu diffusion barrier, N-rich films exhibited much better CV characteristics. This indicates that the optimum BCN bonding for improved electrical performance has yet to be found. Additionally, the Cu barrier tests were performed on 50 nm thick BCN, at least an order of magnitude thicker than what would be allowed in a current IC device. The scalability of the diffusion barrier properties of BCN should be investigated as a function of film thickness.

The current BCN CVD process has been thoroughly explored over the available processing temperatures, pressures, and gas flow rates. To obtain films with lower dielectric constants and less electrical defects, other deposition chemistries should be approached. Specifically, use of a precursor compound without N and C containing ligands would allow for more control over the compositional variation of the process.

Developing an accurate and repeatable methodology for determination of the dielectric constant of these films would aid greatly in determining the direction of future experiments. In the past, Engbrecht was able to measure the dielectric constant of BCN with an industrial mercury probe. Attempts to extract the κ from a benchtop Hg probe as well as using MOS capacitor structures with metal gates deposited by shadowmask and photolithography have failed. The lowest obtainable κ for this BCN is 3.66. When compared to current low κ materials having dielectric constants as low as 2, it is clear that even a thin layer of BCN may raise the effective dielectric constant appreciably. While the forming gas anneal experiments were unsuccessful at enhancing the dielectric properties of BCN, further studies with both UV and thermal annealing of BCN along with FTIR and dielectric measurements could aid in understanding the tunability of these films.

A fully quantitative technique is needed to determine the actual hydrogen content in these films. Transmission FTIR measurements may be converted to quantitative measurements by relating the area of the absorbance peak to the concentration by means of a proportionality constant. These values are known for C-H and N-H vibrations in transmission but may not be extended to ATR FTIR. Elastic recoil detection analysis is a potential quantitative technique for determining the hydrogen content of BCN.

Bibliography

Abdul Mannan, M., Nagano, M., Kida, T., Hirao, N., Baba, Y., *Journal of Physics and Chemistry of Solids*, 70, pp. 20-25; 2009

Afanas'ev, V.V., Stesmans, A., Edge, L.F., Scholm, D.G., Heeg, T., Schubert, J., *Applied Physics Letters*, 88, pp. 032104 1-3; 2006.

Ahearn, W.J., Fitzpatrick, P.R., Ekerdt, J.G., *J. Vac. Sci. Technol. A*, 25, pp. 570-574; 2007.

Akkerman, Z.L., Efstathiadis, H., Smith, F.W., *Journal of Applied Physics*, 80, pp. 3068-3074; 1996.

Akkerman, Z.L., Kosinova, M.L., Fainer, N.I., Rumjantsev, Yu.M., Sysoeva, N.P., *Thin Solid Films*, 260, pp. 150-160; 1995.

Annen, A., Saß, M., Beckmann, R., von Keudell, A., Jacob, W., *Thin Solid Films*, 312, pp. 147-155; 1998.

Anutgan, M., Aliyeva Anutgan, T., Ozkol, E., Atilgan, I., Katircioglu, B., *Journal of Non-Crystalline Solids*, 355, pp. 1622-1629; 2009.

Baklanov, M.R., Maex, K. *Phil. Trans. R. Soc. A*, 364, pp. 201-215; 2006.

Bellamy, L.J., The Infrared Spectra of Complex Molecules. London, England: Chapman and Hall; 1975.

Billa, R.B., Hofmann, T., Schubert, M., Robertson, B.W., *Journal of Applied Physics*, 106, pp. 033515 1-4; 2009.

Bounouh, Y., Thèye, M.L., *Physical Review B*, 51, pp. 9597-9604; 1995.

Broussous, L., Puyrenier, W., Rebiscoul, D., Rouessac, V., Ayral, A., *Microelectronic Engineering*, 84, pp. 2600-2605; 2007.

Carrow, B.P., Murray, R.E., Woods, B.W., Senkevich, J.J., *Mater. Res. Soc. Symp. Proc.*, 863, pp. B2.10.1-6 ; 2005.

Chambers, S.A., Droubay, T., Kaspar, T.C., Gutowski, M., *J. Vac. Sci. Technol. B*, 22, pp. 2205-2215; 2004.

Chang, C.-C., Pan, F.-M., Chen, C.-W., *Microelectronic Engineering*, 86, pp. 2241-2246; 2009.

Chen, X.T., Gui, D., Chi, D.Z., Wang, W.D., Babu, N., Hwang, N., Lo, G.Q., Kumar, R., Balasubramanian, N., Kwong, D.-L., *IEEE Electron. Device Lett.*, 26, pp. 616-618; 2005.

Chen, Z., Prasad, K., Li, C.Y., Lu, P.W., Su, S.S., Tang, L.J., Gui, D., Balakumar, S., Shu, R., Kumar, R., *Appl. Phys. Lett.*, 84, pp. 2442-2444; 2004.

Cheng, Y.-L., Chen, S.-A., Chiu, T.-J., *J. Vac. Sci. Technol. B*, 28, pp. 573-576; 2010.

Chiang, C.-C., Wu, Z.-C., Wu, W.-H., Chen, M.-C., Ko, C.-C., Chen, H.-P., Jang, S.-M., Yu, C.-H., Liang, M.-S. *Jpn. J. Appl. Phys.*, 42, pp. 4489-4494; 2003.

Cho, W., Saxena, R., Roderiguez, O., Ojha, M., Achanta, R., Plawsky, J.L., Gill, W.N., *J. Electrochem. Soc.*, 152, pp. F61-F65; 2005.

Choi, B.H., Lim, Y.H., Lee, J.H., Kim, Y.B., Lee, H.-N., Lee, H.K., *Microelectronic Engineering*, 87, pp. 1391-1395; 2010.

Cunningham, J., *Semiconductor International*, April 2000, pp. 1-8; 2000.

Dalui, S., Pai, A.K., *Vacuum*, 82, pp. 1296-1301; 2008.

Dreer, S., Wilhartitz, P., Piplits, K., Mayerhofer, K., Foisner, J., Hutter, H., *Anal. Bioanal. Chem.*, 379, pp. 599-604; 2004.

Engbrecht, E.R., Cilino, C.J., Junker, K.H., Sun, Y.M., White, J.M., Ekerdt, J.G., *Mater. Res. Soc. Symp. Proc.*, 766, pp. E.8.2.1-6; 2003.

Engbrecht, E.R., Dissertation, The University of Texas at Austin; 2004.

Engbrecht, E.R., Sun, Y.-M., Junker, K.H., White J.M., Ekerdt, J.G., *J. Vac. Sci. Technol. B*, 23, pp. 463-467; 2005.

Engbrecht, E.R., Sun, Y.-M., Junker, K.H., White, J.M., Ekerdt, J.G., *J. Vac. Sci. Technol. A*, 22, pp. 2152-2158; 2004.

Essafti, A., Ech-chamikh, E., Azizan, M., *Spectroscopy Letters*, 41, pp. 57-63; 2008.

Essafti, A., Ech-chamikh, E., Fierro, J.L.G., *Diamond and Related Materials*, 14, pp. 1663-1668; 2005.

Ferrari, A., Rodil, S., Robertson, J., *Physical Review B*, 67, pp. 155306 1-20; 2003.

Fitzpatrick, P.R., Dissertation, The University of Texas at Austin; 2009.

Fitzpatrick, P.R., Ekerdt, J.G., *J. Vac. Sci. Technol. B*, 27, pp. 2366-2374; 2009.

Fitzpatrick, P.R., Satyanarayana, S., Sun, Y.-M., White, J.M., Ekerdt, J.G., *Mater. Res. Soc. Symp. Proc.*, 863, pp. B6.8.1-6; 2005.

Gambino, J., Wynne, J., Gill, J., Mongeon, S., Meatyard, D., Lee, B., Bamnolker, H., Hall, L., Li, N., Hernandez, M., Little, P., Hamed, M., Ivanov, I., Gan, C.L., *Microelectronic Engineering*, 83, pp. 2059-2067; 2006.

Godet, C., Schmirgeld, L., Zuppiroli, L., Sardin, G., Gujrathi, S., Oxorn, K., *Journal of Material Science*, 26, pp. 6408-6418; 1991.

Gosset, L.G., Chun, S., Farcy, A., Casanova, A., Arnal, V., Besling, W.F.A., Torres, J., *Proceedings of the IEEE International Interconnect Technology Conference*, 7-9 June 2004, pp. 15-17; 2004.

Grill, A, Patel, V., *Applied Physics Letters*, 79, pp. 803-805; 2001.

Grill, A., Patel, V., Jahnes, C., *J. Electrochem. Soc.*, 145, pp. 1649-1653; 1998.

Hammer, P., Baker, M.A., Lenardi, C., Gissler, W., *Thin Solid Films*, 290-291, pp. 107-111; 1996.

Henderson, L.B., Ekerdt, J.G., *Thin Solid Films*, 517, pp. 1645-1649; 2009.

Hofmann, S., Rar, A., Moon, D.W., Yoshihara, K., *J. Vac. Sci. Technol. A*, 19, pp. 1111-1115; 2000.

Hohage, J, Lehr, M.U., Kahlert, V., *Microelectronis Engineering*, 86, pp. 408-413; 2009.

Hoyas, A.M., Schuhmacher, J., Whelan, C.M., Baklanov, M.R., Carbonell, L., Celis, J.P., Maex, K., *J. Vac. Sci. Technol. B*, 23, pp. 1551-1557; 2005.

Jezewski, C., Wiegand, C.J., Ye, D., Mallikarjunan, A., Liu, D., Jin, C., Lanford, W. A., Wang, C., Senkevich, J.J., Lu, T.-M., *J. Electrochem. Soc.*, 151; pp. F157-F161; 2004.

Juneja, J.S., Ten Eyck, G.A., *J. Vac. Sci. Technol. B*, 23, pp. 2232-2235; 2005.

Kawaguchi, M., Nozaki, K., Kita, Y., Doi, M., *Journal of Materials Science*, 26, pp. 3926-3930; 1991.

Kraut, E.A., Grant, R.W., Waldrop, J.R., Kowalczyk, S.P., *Phys. Rev. Lett.*, 44, pp. 1620-1623; 1980.

Kumar, R., Wong, T.K.S., Murthy, B.R., Wang, Y.H., Balasubramanian, N., *J. Electrochem. Soc.*, 153, pp. G420-G427; 2006.

Lazzeri, P., Hua, X., Oehrlein, G., Barozzi, M., Iacob, E., Anderle, M. *J. Vac. Sci. Technol. B*, 23, pp. 1491-1498; 2005.

Lee, S., Yang, J., Yeo, S., Lee, J., Jung, D., Boo, J.-H., Kim, H., Chae, H., *Japanese Journal of Applied Physics*, 46, pp. 536-541; 2007.

Lin, S.-H., Feldman, B.J., *Applied Physics Letters*, 69, pp. 2373-2375; 1996.

Ling, H., Wu, J.D., Sun, J., Shi, W., Ying, Z.F., Li, F.M., Diamond and Related Materials, 11, pp. 1623-1628; 2002.

Linss, V., Rodil, S.E., Reinke, P., Garnier, M.G., Oelhafen, P., Kreissig, U., Richter, F., *Thin Solid Films*, 467, pp. 76-87; 2004.

Mannaert, G., Baklanov, M.R., Le, Q.T., Travaly, Y., Boullart, W., Vanhaelemeersch, Jonas, A.M., *J. Vac. Sci. Technol. B*, 23, pp. 2198-2202;2005.

Milella, A., Delattre, J.L., Palumbro, F., Fracassi, F., d’Agostino, R., *Journal of the Electrochemical Society*, 153, pp. F106-F114; 2006.

Mondal, S., Banthia, A.K., *Journal of the European Ceramic Society*, 25, pp. 287-291; 2005.

Morant, C., Prieto, P, Bareno, J., Sanz, J.M., Elizalde, E., *Thin Solid Films*, 515, pp. 207-211; 2006.

Morgen, M., Ryan, E.T., Zhao J.-H., Hu, C., Cho, T., Ho, P.S. *Annu. Rev. Mater. Sci.*, 30, pp. 645-680; 2000.

Moulder, J.F., Stickle, W.F., Sobol, P.E., Bomben,K.D., Handbook of X-ray Photoelectron Spectroscopy. Eden Prairie, MN: Physical Electronics, Inc.; 1995.

Nakano, H., Itabashi, T., Akahoshi, H., *J. Electrochem. Soc.*, 152, pp. C163-C166; 2005.

Patel, Z.P., Roy, A.N.U., Bakhru, H., Lu, T.-M., *Thin Solid Films*, 476, pp. 322-325; 2005.

Perego, M., Seguini, G., Scarel, G., Fanciulli, M., Wallrapp, F., *Journal of Applied Phyics*, 103, pp. 043509-1-6; 2008.

Perng, D.-C., Yeh, J.-B., Hsu, K.-C., Wang, Y.-C., *Electrochem. And Solid-State Letters*, 13, pp. H290-H293; 2010.

Phani, A.R., Manorama, S., Rao, V.J., *Semicond. Sci. Technol.*, 10, pp. 1520-1522; 1995.

Plummer, J.D., Deal, M.D., Griffin, P.B. Silicon VLSI Technology Fundamentals, Practice and Modeling. Upper Saddle River, NJ: Prentice Hall; 2000.

Podder, J., *Modern Physics Letters B*, 21, pp. 455-466; 2007.

Posseme, N., Chevolleau, T., David, T., Darnon, M., Louveau, O., Joubert, O., *J. Vac. Sci. Technol. B*, 25, pp. 1928-1940; 2007.

Saß, M., Annen, A., Jacob, W., *J. Appl. Phys.*, 82, pp. 1905-1908; 1997.

Schulz, D.L., Lutfurakhmanov, A., Mayo, B., Sandstrom, J., Bunzow, D., Qadri, S.B., Bao, R., Chrisey, D.B., Caruso, A.N., *J. Non-Crystalline Solids*, 354, pp. 2369-2371; 2008.

Senkevich, J.J., Jezewski, C., Lu, D., Lanford, W.A., Wang, G.-C., Lu, T.-M., *Mater. Res. Soc. Symp. Proc.*, 812, pp. F1.21-10; 2004.

Speranza, G., Minati, L., *Diamond and Related Materials*, 16, pp. 1321-1324; 2007.

Stein, H.J., Wegener, H.J.R, *J. Electrochem. Soc.*, 124, pp. 908-912; 1977.

Strittmatter, R.J., Hahnfeld, J.L., Silvis, H.C., Stokich, T.M., Perry, J.D., Ouellette, K.B., Niu, Q.J., Godschalx, J.P., Kalantar, T.H., Mubarekyan, E., Hefner, Jr., R.E., Lyons, J.W., Dominowski, J.M., Buske, G.R., *Mater. Res. Soc. Symp. Proc.*, 766, pp. E.7.5.1-8; 2003.

Sugino, T., Tai, T., Etou, Y., *Diamond Relat. Mater.*, 10, pp. 1375-1379; 2001.

Sugiyama, T., Tai, T., Sugino, T., *Applied Physics Letters*, 80, pp. 4214-4216; 2002.

Tai, T., Sugiyama, T., Sugino, T., *Diamond Relat. Mater.*, 12, pp. 1117-1121; 2003.

Takewaki, T., Yamada, H., Shibata, T., Ohmi, T., Nitta, T., *Proceedings of the International Symposium on Power Semiconductor Devices and ICs*, 23-25 May 1995, pp. 438-442; 1995.

Titus, E., Misra, D.S., Sikder, A.K., Tyagi, P.K., Singh, M.K., Misra, A., Ali, N., Cabral, G., Neto, V.F., Gracio, J., *Diamond & Related Materials*, 14, pp. 476-481; 2005.

Tokuyama, S. Hara, M., Kabir, M., Watanabe, D., Kimura, C., Aoki, H., Sugino, T., *Japanese Journal of Applied Physics*, 47, pp. 2492-2495; 2008.

Travaly, Y., Schuhmacher, J., Baklanov, M.R., Giangrandi, S., Richard, O., Brijs, B., Van Hove, M., Maex, K., Abell, T., Somers, K.R.F., Hendrickx, M.F.A., Vanquickenborne, L.G., Ceulemans, A., Jonas, A.M., *J. Appl. Phys.*, 98, pp. 083515-1-9; 2005.

Umeda, S., Yuki, T., Sugiyama, T., Sugino, T., *Diamond and Related Materials*, 13, pp. 1135-1138; 2004.

Volksen, W., Miller, R.D., Dubois, G. *Chem. Rev.*, 82, pp. 56-110; 2010.

von Keudell, A., Jacob, W., *J. Vac. Sci. Technol. A*, 15, pp. 402-407; 1997.

von Keudell, A., *Thin Sold Films*, 402, pp. 1-37; 2002.

Vrtis, R.N., O'Neill, M.L., Vincent, J.L., Lukas, A.S., Peterson, B.K., Bitner, M.D., Karwacki, E.J., *Mater. Res. Soc. Symp. Proc.*, 766, pp. E.7.4.1-6; 2003.

Wang, Q., Ekerdt, J.G., Gay, D., Sun, Y.-M., White, J.M., *Appl. Phys. Lett.*, 84, pp. 1380-1382; 2004.

Wexler, A.S., *Applied Spectroscopy Reviews*, 1, pp. 29-98; 1967.

Xu, J., Moxom, J., Yang, S., Suzuki, R., Ohdaira, T., *Appl. Surf. Science*, 194, pp. 189-194; 2002.

Yasui, H., Awazu, K., Ikenaga, N., Sakudo, N., *Vacuum*, 83, pp. 582-584; 2009.

Yue, J., Cheng, W., Zhang, X., He, D., Chen, G., *Thin Solid Films*, 375, pp. 247-250; 2000.

Vita

Wesley James Ahearn was born November 18, 1980, in Panama City, FL. He graduated from Rutherford High School and earned a B.S. in chemical engineering before beginning graduate study at The University of Texas at Austin. Throughout his experiences in graduate school, Wes has retained a healthy curiosity of the world. He looks forward to his next adventure.

Permanent address: c/o The Ahearn Family, 1202 Venetian Way, Panama City, FL 32405
This thesis was typed by the author.